UNIVERSITY OF CALIFORNIA SAN DIEGO

Actuation for Bioinspired, Soft, Swimming Robots

A dissertation submitted in partial satisfaction of the
requirements for the degree
Doctor of Philosophy

in

NanoEngineering

by

Caleb Christianson

Committee in charge:

Professor Michael T. Tolley, Chair
Professor Shengqiang Cai
Professor Henrik Christensen
Professor Darren Lipomi
Professor Joseph Wang
Professor Sheng Xu

2019

The dissertation of Caleb Christianson is approved, and it is acceptable in quality and form for publication on microfilm and electronically:

_____

_____

_____

_____

_____

_____
Chair

University of California San Diego

2019

DEDICATION

I dedicate this dissertation to my wife. Nicole, we did it.

EPIGRAPH

Only a life lived for others is a life worthwhile.

—Albert Einstein

I was born not knowing and have had only a little time to change that here and there.

—Richard Feynman

TABLE OF CONTENTS

LIST OF FIGURES

LIST OF TABLES

ACKNOWLEDGEMENTS

I would like to begin by sharing my appreciation for my funding sources, without which the following would have been impossible: the Charles Lee Powell Foundation, the National Science Foundation Graduate Research Fellowship Program, the Office of Naval Research, and viewers like you.

To Michael Tolley, thank you for your years of guidance, advice, patience, encouragement, and mentorship. Thank you for everything that you've taught me, both in the lab and on the water.

To my committee, thank you for your time and support throughout my studies. Prof. Cai, thank you for all of your help with DEAs. Prof. Christensen, thank you for sharing your expertise on robotics and for all of your support with RoboGrads. Prof. Lipomi, thank you for your invaluable lessons on everything from intermolecular forces to professional development. Prof. Wang, thank you for taking me under your wing during my first year at UC San Diego and for letting me be a part of your team and exciting research. Prof. Xu, thank you for sharing your enthusiasm and insight on stretchable electronics.

To the members and alumni of the Bioinspired Robotics and Design Lab: thank you for every lesson that you've taught me, every meal and drink that we've shared, and for all of your help and encouragement along the way. I couldn't have done this without your help and support. Ben, I'm glad we were able to collaborate on the sensor projects and I'm thankful for all that we were able to do together with RoboGrads. Thank you for helping me every time I got stuck with a microcontroller and for helping me to learn how to swim. Dylan, thank you for being so upbeat and for being a tireless source of

encouragement, high fives, and new ideas. Also, thank you for helping me learn how to surf and for getting me hooked on Tourmaline. Shea, thank you for introducing me to surfing and for taking me out for my first two sessions on your spare board. Will, thank you for playing with words with me. Adriane, I'm glad for our shared enthusiasm of both good BBQ and smart materials. Saurabh, thank you for the late-night/early morning VR sessions and for regularly being able and willing to teach me something new from your incredible depth of knowledge. Emily, thank you for encouraging me to be more active and for always being willing to help. Ishida, thank you for always being there for an enjoyable luncthime conversation or drink and for always having a keen, helpful perspective. Jessica, thank you for sharing your energy and enthusiasm in everything that you explore. Paul, thank you for your advice and for your demonstration on how to be a better engineer and overall person. Iman, thank you for knowing how to make me laugh and for being such a gracious, patient student. Nancy, thank you for helping me with homework problems and for the tea (which has helped me write this dissertation).

To the members and alumni of Prof. Wang's lab, thank you for welcoming me to UCSD and for being a continued source of friendship and encouragement throughout my time here. Special thanks to the 2014 cohort of Fernando, Itthipon, and Rajan: we've all come and gone a long way since then, but it's been good to go through all of it with you.

To all of the students that have allowed me to try to provide some mentorship along the way: thank you for everything that you taught me and for all of your help and hard work. None of this would have turned out as well as it has without all of your help. In particular, I would like to thank Nate for teaching me about working carefully and precisely, Kyle for his tireless creative efforts, and Yi for always being on top of things

and for continually exceeding my expectations.

To Dana, thank you for being such an upbeat source of guidance throughout my time at UCSD. You have been the most consistently kind, helpful, supportive, encouraging person throughout my time at UCSD. To David, thank you for being so kind, encouraging, and upbeat. Thank you to Shawn and Ashley from Konos and to Jason from Cups for keeping me caffeinated. Thank you to the Newbreak Young Professionals crew for the wisdom and encouragement throughout my time in San Diego. Special thanks to James, Steve, and Enrique for teaching me how to surf. Thanks to James, Derrick, and Joey for advice on professional development. And thanks to Heather, Tucker, Hannah, and Enrique for being some of the best friends that I've ever had and for being some of the finest people that I've ever met. To the friends at Tourmaline, thank you for making room for my car and for sharing your joy with me. Thanks to Tom for a roof over my head and to Lon for three wheels under my feet. Special thanks goes out to every dog that I've ever met. To Jasper, who helped me through so much of this journey, I wish we were able to spend just a little more time together so that you could celebrate this with me too.

To Dr. Wu, ten years ago I came to your office as a homeschooled freshman who just quit his job at a gas station. I shared my passion for nanotechnology with you and you were kind enough to take me in. You taught me what it meant to do good research and you laid the foundation for my PhD. I would not be where I am without your guidance, patience, and instruction. To Caitlin, thank you for teaching me how to write better and for helping me to also win the NSF. To Alan, thank you for helping me navigate both the engineering physics program and preparing me for graduate school. Not sure if this fits our bet or not, but it looks like I'll publish an exclamation point before you do!

To my parents, thank you for raising me and allowing and encouraging me to pursue myriad interests. Mom, thank you for being my teacher and coach. Dad, thank you for teaching me discipline and the importance of hard work.

To Nicole, the reason why I began on this journey and the reason why I've been able to complete it. Thank you for being so kind, patient, flexible, adventurous, and supportive throughout our journey together. I love you more than I know how to describe in words. I can't wait to see where the next chapter of our life together leads.

If you're reading this and I haven't named you, thank you for your patience, your kindness, and for being you. If we've met, my life is better for it. If we have yet to meet, I look forward to the day.

The following acknowledgements are to satisfy the requirements of the University of California San Diego.

Chapter 1, in full, is a reprint of the material as it appears in Science Robotics, 2018. Christianson, Caleb; Goldberg, Nathaniel N.; Deheyn, Dimitri D.; Cai, Shengqiang; Tolley, Michael T., Science 2018. The dissertation author was the primary investigator and author of this paper.

Chapter 2, in full, has been submitted for publication of the material. Christianson, Caleb; Bayag, Christopher; Li, Guorui; Jadhav, Saurabh; Giri, Ayush; Agba, Chibuike; Li, Tiefeng; Tolley, Michael T. The dissertation author was the primary investigator and author of this paper.

Chapter 3, in full, has been submitted for publication of the material. Christianson, Caleb; Cui, Yi; Bi, Xiaobo; Zhu, Qiang; Pawlak, Geno; Tolley, Michael T. The dissertation author was the primary investigator and author of this paper.

VITA

2014	B. S. in Engineering Physics, University of Kansas
2015	M. S. in NanoEngineering, University of California San Diego
2019	Ph. D. in NanoEngineering, University of California San Diego

PUBLICATIONS

[1] **C. Christianson**, Y. Cui, X. Bi, Q. Zhu, G. Pawlak, and M. T. Tolley, "Cephalopod-inspired robot capable of cyclic jet propulsion through shape change," submitted for publication.

[2] **C. Christianson**, C. Bayag, G. Li, S. Jadhav, A. Giri, C. Agba, T. Li, and M. T. Tolley, "Jellyfish-inspired soft robot driven by fluid electrode dielectric organic robotic actuators," submitted for publication.

[3] B. Shih, **C. Christianson**, K. Gillespie, S. Lee, J. Mayeda, Z. Huo, and M. T. Tolley, "Design Considerations for 3D Printed, Soft, Multimaterial Resistive Sensors for Soft Robotics," *Frontiers in Robotics and AI*, vol. 6, no. April, pp. 1–12, 2019.

[4] **C. Christianson**, N. N. Goldberg, D. D. Deheyn, S. Cai, and M. T. Tolley, "Translucent soft robots driven by frameless fluid electrode dielectric elastomer actuators," *Science Robotics*, vol. 3, p. eaat1893, apr 2018.

[5] **C. Christianson**, N. N. Goldberg, and M. T. Tolley, "Elastomeric diaphragm pump driven by fluid electrode dielectric elastomer actuators (FEDEAs)," *Electroactive Polymer Actuators and Devices (EAPAD) XX*, no. March, p. 21, 2018.

[6] **C. Christianson**, N. Goldberg, S. Cai, and M. T. Tolley, "Fluid electrodes for submersible robotics based on dielectric elastomer actuators," in *Electroactive Polymer Actuators and Devices (EAPAD) XIX*, p. 101631O, 2017.

[7] K. Kumar, J. Liu, **C. Christianson**, M. Ali, M. T. Tolley, J. Aizenberg, D. E. Ingber, J. C. Weaver, and K. Bertoldi, "A Biologically Inspired, Functionally Graded End Effector for Soft Robotics Applications," *Soft Robotics*, vol. 4, p. soro.2017.0002, 2017.

[8] B. Shih, D. Drotman, **C. Christianson**, Z. Huo, R. White, H. I. Christensen, and M. T. Tolley, "Custom soft robotic gripper sensor skins for haptic object visualization," in *IEEE International Conference on Intelligent Robots and Systems*, pp. 494–501, 2017.

[9] M. B. Quadrelli, H. Garrett, J. Castillo, A. Stoica, M. Ono, **C. Christianson**, D. Lusso, and H. Schaub, "Active electrostatic flight for airless bodies," in *IEEE Aerospace Conference Proceedings*, pp. 1–16, 2017.

[10] A. Minori, B. Shih, **C. Christianson**, and M. T. Tolley, "3D Printed Shape Memory Polymer Composite for Fabric Actuation," in *Robot Makers 2 Workshop, Robotics: Science and Systems (RSS)*, 2016.

[11] Z. Wu, B. Esteban-Fernández de Ávila, A. Martín, **C. Christianson**, W. Gao, S. K. Thamphiwatana, A. Escarpa, Q. He, L. Zhang, and J. Wang, "RBC micromotors carrying multiple cargos towards potential theranostic applications," *Nanoscale*, vol. 7, no. 32, pp. 13680–13686, 2015.

[12] R. Dong, J. Li, I. Rozen, B. Ezhilan, T. Xu, **C. Christianson**, W. Gao, D. Saintillan, B. Ren, and J. Wang, "Vapor-Driven Propulsion of Catalytic Micromotors," *Scientific Reports*, vol. 5, p. 13226, 2015.

[13] Z. Wu, T. Li, J. Li, W. Gao, T. Xu, **C. Christianson**, W. Gao, M. Galarnyk, Q. He, L. Zhang, and J. Wang, "Turning erythrocytes into functional micromotors," *ACS Nano*, vol. 8, no. 12, pp. 12041–12048, 2014.

[14] M. Choate, J. Meeth, **C. Christianson**, P. Collins, and C. Depcik, "A Swappable Battery Pack for Short-Range Electric Vehicles," 2014.

[15] **C. Christianson**, R. Lu, and J. Wu, "Dimension effect on the performance of carbon nanotube nanobolometers," *Nanotechnology*, vol. 25, no. 42, p. 425503, 2014.

[16] R. Lu, **C. Christianson**, B. Weintrub, and J. Z. Wu, "High photoresponse in hybrid graphene-carbon nanotube infrared detectors," *ACS Applied Materials and Interfaces*, vol. 5, no. 22, pp. 11703–11707, 2013.

[17] R. Lu, **C. Christianson**, A. Kirkeminde, S. Ren, and J. Wu, "Extraordinary photocurrent harvesting at type-II heterojunction interfaces: Toward high detectivity carbon nanotube infrared detectors," *Nano Letters*, vol. 12, no. 12, pp. 6244–6249, 2012.

[18] R. Lu, **C. Christianson**, J. Dizon, J. Wu, T. Haugan, P. Barnes, and F. J. Baca, "Investigation of Dynamic Behaviors of Low-Level Dissipation at YBa2Cu3O7 Grain Boundaries Using Low-Temperature Near-Field Scanning Microwave Microscopy," *IEEE Transactions on Applied Superconductivity*, vol. 21, no. 3, pp. 3238–3242, 2011.

ABSTRACT OF THE DISSERTATION

Actuation for Bioinspired, Soft, Swimming Robots

by

Caleb Christianson

Doctor of Philosophy in NanoEngineering

University of California San Diego, 2019

Professor Michael T. Tolley, Chair

It is often impractical or dangerous to send people to explore underwater environments. In these situations, it is preferable to send robots such as autonomous underwater vehicles or remotely operated vehicles instead. Unfortunately, robots impart their own risks: they are typically made of rigid materials that can become lodged in confined spaces or harm underwater creatures and structures. Additionally, propellers or jet thrusters are typically used for propulsion, which are power intensive, have low efficiency, and impose additional concerns of entanglement and damage to their environment. Finally, they generate considerable noise and vibration, thus adding to the ambient noise pollution and disturbing sea life, preventing researchers from being able to study more timid animals. In

this dissertation, I describe physical mechanisms to develop bioinspired, soft, swimming robots with an emphasis on actuation. First, I present an approach to use an arrangement of six artificial muscles based on dielectric elastomer actuators (DEAs) to actuate a tethered robot capable of anguilliform-inspired locomotion. Next, I demonstrate pulsatile, jellyfish-inspired locomotion using DEAs with a simpler actuation and control strategy, enabling an untethered, soft, swimming robot. Finally, I explore an alternative actuation approach to achieve more robust locomotion in a cephalopod-inspired robot based on slowly storing elastic energy and then quickly releasing it to eject a pulsed jet for propulsion. The first two robots are silent and use actuators that have a high energy density and efficiency, but provide low output power and swim at low speeds. In the cephalopod-inspired robot, we trade silence and efficiency for power and speed. These results demonstrate actuation strategies for realizing bioinspired locomotion in soft, swimming robots that could be useful for structural diagnostics, environmental monitoring, or search and rescue.

INTRODUCTION

Overview

My dissertation is designed to answer three hypotheses: 1) how can we use dielectric elastomer actuators (DEAs) in underwater environments; 2) how can we optimize DEAs with fluid electrodes for pulsatile, periodic motion to enable untethered, underwater propulsion; and 3) how can we generate the shape-change required for high-power jet propulsion. I explore and test these hypotheses through three experimental robots.

Fluid electrodes for dielectric elastomer actuators

Dielectric elastomer actuators (DEAs) are a type of artificial muscle based on an electroactive polymer [1, 2]. DEAs comprise a thin, elastomeric membrane that is sandwiched by two compliant electrodes [3]. When one applies a voltage to the electrodes, electrostatic forces will deform the membrane as charges accumulate on either side of the membrane. This force, known as Maxwell stress, is generated by charges that build up on the surfaces of the membrane, resulting in a reduction of thickness as the charges of opposite signs attract. For an incompressible material, the reduction in thickness, coupled with the repulsion of like charges on the surfaces, result in an increase in area. These actuators are known for their speed (up to 10s of kHz) [4], high energy density (3400 J/kg) and energy conversion efficiency (up to 90%) [5], and large strains (up to 2200%) [6]. One of the key challenges with making DEAs practical is in the choice of a suitable electrode materials. The electrodes must be thin and compliant, as a thick, stiff electrodes will reduce or eliminate the actuation [7]. The most common choices for electrodes for DEAs are typically carbon-based powders (e.g., carbon nanotubes) [8], carbon particles embedded in a silicone grease (carbon grease) [9], or carbon particles suspended in a polymer matrix

(e.g., carbon in polydimethylsiloxane, cPDMS) [10, 11]. Alternatively, some groups have worked on using conductive hydrogels as an electrode material [4, 12]. One challenge with using either carbon-based or hydrogel electrodes for DEAs in underwater applications is that the electrodes must be encapsulated to prevent damage to the electrodes caused by abrasion and to prevent the electrodes from shorting out to the surrounding fluid [13]. The use of an encapsulation layer will stiffen the overall structure, reducing its performance. To increase the performance of submersible DEAs, I hypothesized that if the surrounding fluid was conductive and grounded, it could be used as the ground electrode of the DEA, thus reducing the complexity and stiffness of the actuator. This was supported by other groups who used the surrounding fluid for the ground electrode of their DEA-based swimming robots [12, 14]. In addition, I hypothesized that if fluid could be used for the ground electrode, that an actuator could be developed using fluid for the high voltage electrode as well. To demonstrate that fluid (in this case, water) can be an effective electrode material, I developed an eel- and a jellyfish-inspired robot that are comprised of fully compliant materials, aside from the driving electronics. To achieve the types of motion found in eels and jellyfish, an additional approach that I employed was to use prestrain-free membranes for my actuators. Early research demonstrated that the performance of DEAs improved when the membranes are prestrained and affixed to a rigid frame [2]. While there are a number of advantages of using prestrained films (e.g., higher strains, reduced risk of electromechanical instability and failure of the film), the use of a prestrained film necessitates a rigid or semi-rigid frame to hold the prestrain in the film. The use of a frame would stiffen the structure, thus making it more challenging to achieve similar motion as those found in soft, swimming animals.

Cyclic jet propulsion based on slow storage and rapid release of elastic energy

At low speeds, squid and cuttlefish use undulating fins to swim. However, for high speed swimming or escape maneuvers, cephalopods employ pulsed jet propulsion [15]. To achieve locomotion, they intake water into their mantle cavity and then eject it out through a nozzle. They can repeat this process cyclically to achieve pulsed jet propulsion. Interestingly, research has shown that pulsed jets can be 50% more efficient than a steady jet [16]. In addition, cephalopods can achieve an additional acceleration from the added mass effect as they decrease their overall volume during the jet period [17, 18]. Previous research has demonstrated the effectiveness of the added mass effect [19] and cyclic, pulsed jet propulsion [20] in cephalopod-inspired robots, but developing an untethered platform that can effectively demonstrate the culmination of both concepts remained an open challenge.

In chapter one, I explore the use of fluid electrodes for DEAs. I present an analytical model to describe the motion of the actuators based on the material, voltage, and geometry of the actuators and compare the model to experimental results. I also characterize the translucency of the actuators, enabling passive camouflage, and their ability to be used for visual communication. Additionally, I demonstrate that the actuators can be completely silent, thus demonstrating their efficacy in applications where low-vibration or stealth is desired. Finally, I integrate three pairs of antagonistic actuators into a robot and demonstrate eel-inspired swimming by controlling the actuation sequence of the artificial muscles.

One challenge with the eel-inspired robot is that the complexity of the control electronics and swimming performance of the robot did not lend itself well to untethered swimming. In chapter two, I expand on the work in chapter one to develop an untethered,

swimming robot based on the pulsatile motion of a jellyfish. Instead of pairs of antagonistic actuators to generate a travelling wave in the structure of the robot, I develop a unimorph actuator comprised of a DEA affixed to an inextensible, strain-limiting layer. When I apply a voltage to the DEA, the actuator bends towards the strain-limiting side. I test the performance of DEA unimorph actuators for different thicknesses and stiffnesses of the strain-limiting layer and compare it to experimental results. Finally, I develop a jellyfish-inspired robot based on an axisymmetric array of unimorph actuators and a waterproof, high voltage power supply and demonstrated untethered swimming of the robot.

In chapter three, I develop an actuation approach that enables the repeatable slow storage and fast release of elastic energy in a cephalopod-inspired robot. The robot comprises an axisymmetric array of compliant beams that I covered with an elastomeric skin. I affix either end of the beams to rigid endplates. One end-plate holds a rack, while the other has a motor mount that holds a DC (direct current) motor affixed with a slip gear. As the motor spins the gear, the gear travels up the rack, pulling the two end plates closer together, storing elastic energy in the beams and skin while increasing the volume of the robot. When the motor rotates the gear to the slip-point, the elastic restoring force drives the two endplates apart, decreasing the constrained volume and ejecting a jet of water. This process is repeated cyclically to achieve repeatable, pulsed jet propulsion. A critical parameter in jet propulsion is the ratio of the volume of the ejected fluid to the diameter of the nozzle, with a value of 4 corresponding to a maximum in efficiency when starting from rest [21]. I demonstrate the importance of the size of the nozzle diameter for the volume of ejected fluid through a measurement of the thrust force and a qualitative characterization of the structure of the vortex rings using flow visualization experiments as a function

of both frequency and nozzle diameter. Next, I develop a waterproof power supply and demonstrate free-swimming of the robot and compare the speed of the robot for different nozzle diameters (formation numbers). Finally, as a proof-of-concept demonstration, I demonstrate controlled turning of the robot through thrust vectoring.

This dissertation begins by exploring the use of DEAs with fluid electrodes to enable underwater propulsion based on anguilliform motion. I then tune DEAs with fluid electrodes for pulsatile motion to realize an untethered, jellyfish-inspired robot. Finally, I explore an alternative actuation approach to achieve high power, pulsatile locomotion based on cephalopod-inspired jet propulsion and the added mass effect. This work is an exploration of actuation strategies for achieving effective underwater propulsion in robots with compliant bodies. These results enable future research in developing actuators for robotic platforms that can be tuned for low power consumption, stealth, compliance, transparency, or speed, depending on what type of performance is required. As such, these robots enable platforms for unobtrusive environmental exploration, low power structural monitoring, or search and rescue.

Chapter 1

Translucent Soft Robots Driven by Frameless Fluid Electrode Dielectric Elastomer Actuators

Caleb Christianson,[1] Nathaniel N. Goldberg,[2] Dimitri D. Deheyn,[3] Shengqiang Cai,[4,5] and Michael T. Tolley[4,5]*

[1]Department of NanoEngineering, University of California San Diego, 9500 Gilman Dr., La Jolla, CA 92093.

[2]Department of Mechanical Engineering, University of California, Berkeley, 6141 Etcheverry Hall, Berkeley, CA 94720.

[3]Marine Biology Research Division, Scripps Institution of Oceanography, 9500 Gilman Dr., La Jolla, CA 92093.

[4]Department of Mechanical and Aerospace Engineering, University of California San

Diego, 9500 Gilman Dr., La Jolla, CA 92093.

[5]Materials Science and Engineering Program, University of California San Diego, 9500 Gilman Dr., La Jolla, CA 92093.

Abstract

Dielectric elastomer actuators (DEAs) are a promising enabling technology for a wide range of emerging applications, including robotics, artificial muscles, and microfluidics. This is due to their large actuation strains, rapid response rate, low cost and noise, high energy density, and high efficiency when compared to alternative actuators. These properties of DEAs make them ideal for the actuation of soft submersible devices, although their use has been limited due to three main challenges: (1) developing suitable, compliant electrode materials, (2) the need to effectively insulate the actuator electrodes from the surrounding fluid, and (3) the rigid frames typically required to pre-strain the dielectric layers. Here, we explore the use of a novel frameless, submersible DEA design that uses an internal chamber filled with liquid as one of the electrodes, and the surrounding environmental liquid as the second electrode, thus simplifying the implementation of soft, actuated submersible devices. We demonstrate the feasibility of this approach with a prototype swimming robot—composed of transparent bimorph actuator segments—inspired by the transparent eel larvae, *leptocephalus*. This design achieves undulatory swimming with a maximum forward swimming speed of 1.9 mm/s and a Froude efficiency of 52%. We also demonstrate the capability for camouflage and display through the body of the robot which has an average transmittance of 94% across the visible spectrum, similar to *leptocephalus.* These results suggest the potential for DEAs with fluid electrodes to serve

as artificial muscles for quiet, translucent, swimming soft robots for applications including surveillance and the unobtrusive study of marine life.

INTRODUCTION

Dielectric elastomer actuators (DEAs) show considerable potential in a variety of fields including microrobotics [1, 22], bioinspired robotics [23–25], artificial muscles [5], and microfluidics [10, 26, 27]. Their high energy efficiency and large active strains make them suitable for many applications that require low-power actuators with large strokes. Two recent efforts by Godaba et al. and Shintake et al. have developed underwater swimming actuation with DEAs in jellyfish- and fish-inspired robots [13, 28]. In their most basic form, DEAs are comprised of an elastomeric dielectric sandwiched between a pair of compliant electrodes. The dielectric layer is typically a silicon- or acrylic- based polymer (e.g., polydimethylsiloxane (PDMS) or the acrylic adhesive VHB by 3M, respectively) [2, 3]. The electrodes are generally comprised of deposited metals [7, 29]; carbon particles or nanotubes attached directly to the surface, suspended in a silicone oil, or polymer matrix [7]; ionogels [30, 31]; or ionic hydrogels [4, 12]. However, challenges remain with using the aforementioned approaches to compliant electrodes for transparent swimming robots. Metallic electrodes provide excellent conductivity but add stiffness to the structure, which impedes the actuation [7]. While techniques exist to fabricate metallic films that are flexible and stretchable [32–35], these approaches require complex fabrication procedures and lead to at least partially opaque conductive layers. It is possible to make stretchable metallic electrodes using various methods, however these methods still result in a stiff layer relative to the dielectric layer. As a result, most previous work has used electrodes made of suspensions of carbon in soft or liquid carrier, or of conductive

hydrogels. Carbon particles suspended in a silicone oil (e.g., carbon grease) is the material most commonly used for DEA electrodes, but is challenging to pattern, prone to mechanical abrasion, and opaque. Moreover, carbon grease electrodes are subject to drying and diffusion of the silicone oil through the dielectric layer, which can swell the elastomer and affect the mechanical properties of the DEA over time [7]. While non-polar liquids are known to induce swelling in dielectric elastomers, polar liquids are known to have a much higher compatibility with silicone elastomers and induce minimal swelling [36, 37]. Previous work has demonstrated the patterning of ionic hydrogels to serve as optically transparent electrodes [4, 12, 38]. However, ionic hydrogel electrodes require encapsulation to prevent mechanical abrasion [39] and dehydration [4, 39]. Further, any conductive electrode with non-negligible stiffness reduces the efficiency of the DEA [40], and thus the performance of the actuator. Ionic fluids represent an inexpensive, compliant, and transparent alternative for DEA electrodes [37]. Fluidic electrodes have been used in DEAs to induce buckling of elastomer films on a microfluidic chip [27]; in a thickened electrolyte solution for planar actuators [9]; and for one of the two electrodes in a pressurized ballooning actuator [41], a bimorph actuator [42], and a fast moving electronic robotic fish [12]. Ionic fluid electrodes are especially interesting for use with DEAs in underwater environments, or for fluid applications. The swimming DEAs presented by Godaba et al. [28] and Shintake et al. [13] rely on carbon-based electrodes, requiring the need for encapsulation layers and patterned electrode pairs found in both designs, imparting additional stiffness due to the electrode and encapsulation layers. A recent, hybrid approach combining both hydrogel and fluid electrodes demonstrated a fast moving, soft electronic fish in which hydrogels served as one of the electrodes in a DEA and the surrounding fluid

was used as the ground electrode (Li et al., 2017) [12]. However, this hybrid approach relies on hydrogel electrodes for the internal conductor and the pre-strained actuator necessitates a relatively rigid frame to maintain this pre-strain. We previously presented a simple frameless proof-of-concept bimorph actuator that showed some underwater motion and was straightforward and inexpensive to fabricate, consisting of water for electrodes and pre-strain-free dielectric layers [42]. However, this actuator was powered by a single pair of DEA modules, and thus required a stiffer leading edge to generate asymmetric motion. Further, forward propulsion was only observed when the actuator pushed off the air-water interface during each stroke. The transparency of both fluid and hydrogel electrodes suggest their potential for camouflaged applications, as recently demonstrated by the work of Li et al. [12] and Yuk et al. [43]. The transparency of their devices enables passive camouflage, which eliminates the need for foreknowledge and adaptation to the background and surrounding environment, as required in active camouflage. In addition to camouflaged robotics, even partially transparent actuators open up a suite of promising applications, including flexible displays with haptic feedback or optic applications [44].

In this paper we present a swimming robot inspired by leptocephali (Fig. 1.1) comprised of frameless, transparent, bimorph DEA segments with fluid electrodes. We build upon our previous demonstration of a simple fluid electrode dielectric elastomer actuator (or FEDEA) bimorph [42] and demonstrate that a polar fluid, even one with low conductivity, can be used for both electrodes, obviating the need for hydrogel, carbon-based, or metallic electrodes. We present a new approach to the design and fabrication of submerged actuators in which both electrodes are fluids and the surrounding fluid serves as the second electrode, eliminating the need for patterning and fabricating both electrodes, which

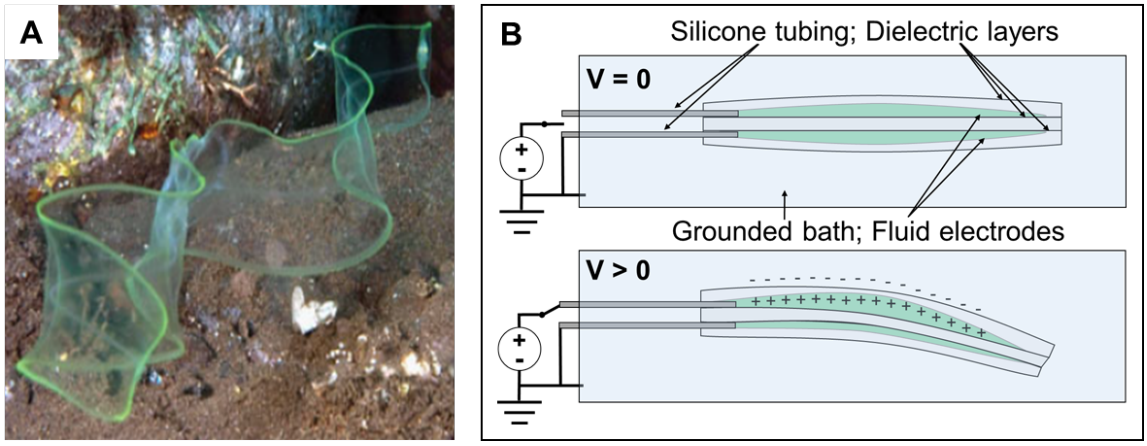

Figure 1.1: Bioinspiration and working principle of FEDEA. A) Photograph of leptocephalus (eel larvae; size about 400 mm in length) swimming underwater. Reprinted from Miller et al. (59), with permission from the authors. B) Working principle of FEDEA bimorph module (not to scale): For bidirectional actuators, we make two DEAs from three layers of an acrylic elastomer adhesive. We create the active areas of the actuators by selectively passivating the surfaces of the adhesive with a powder, which allows the conductive fluid to enter from the tubing and cover the active area. We connect the actuator to the high voltage lead of the power supply through the silicone tubing. Application of a voltage in one of the fluid chambers with respect to the external fluid induces a Maxwell stress in the dielectric, inducing a bending motion away from the actuated side.

has been required in most previous DEAs. This simplifies the design of the actuators and improves their efficiency by eliminating the need to add conductive and encapsulation layers that would stiffen the DEA. Since the fluid electrodes and dielectric elastomer are translucent, so is our swimming robot, enabling passive camouflage and optical communication. We achieve this with pre-strain-free DEAs, eliminating the need for rigid frames to maintain the pre-strain, resulting in a fully compliant actuator capable of continuous deformation. We demonstrate this approach with a proof-of-concept implementation of FEDEAstranslucent bimorph actuators for a submersible swimming soft robot.

RESULTS

Design of an FEDEA bimorph module

We designed and fabricated FEDEA bimorphs consisting of two separate fluid chambers enclosed by three layers of dielectric elastomer (Fig. 1.1B, Fig. 1.5). When we submerged the actuator in a grounded fluid and applied a voltage to one of the fluid chambers in the actuator with respect to ground, the Maxwell pressure compressed the dielectric layer between the internal fluid and the external bath. This induced the chamber to elongate in the directions perpendicular to the electrical field, which caused the bimorph to bend away from the actuated side.

Analytical bending model

To develop an understanding of how the actuation of our bimorph module scales with its geometry, material properties, and the applied voltage, we employ elementary Euler-Bernoulli beam theory. We consider the actuator to be a collection of three layers of equal thickness h stacked on top of one another and examine the case in which one of the outer two layers is actuated, i.e. the case where the bimorph undergoes a bending deformation, either upward or downward.

When a voltage is applied across one of the layers, opposing charge distributions build up on either side, causing an effective mechanical pressure p, which in turn results in a longitudinal strain in said layer. An application of Hooke's law shows that this strain is given by

$$\varepsilon_{xx} = \frac{\nu p}{E} \tag{1}$$

where ε_{xx} and E are Poisson's ratio and elastic modulus of the dielectric elastomer, respectively. Pelrine's equation [2] gives an expression for the equivalent mechanical pressure acting on the actuated layer:

$$p = \epsilon_0 \epsilon_r \left(\frac{V}{h}\right)^2. \tag{2}$$

Here, ϵ_0 is the permittivity of free space, ϵ_r the relative permittivity of the dielectric elastomer, and V the applied voltage. We now analyze the bimorph as a whole, approximating the collection of three layers as an Euler-Bernoulli beam of thickness $3h$ undergoing pure bending. It follows that the longitudinal strain is y/ρ, where y is the distance from the neutral axis. Considering Eq. 1 to be the leading-order expression for the longitudinal strain in the extreme tensile fiber of the beam, we find, after dropping a constant of $3/2$ that

$$\frac{h}{\rho} \sim \frac{\nu p}{E} \ . \tag{3}$$

By inserting Eq. 2 into Eq. 3 and rearranging, we find the leading-order functional dependence of the curvature to be

$$\frac{1}{\rho} \ \sim \ \frac{\nu \epsilon_0 \epsilon_r V^2}{E h^3} \ . \tag{4}$$

This result suggests that the curvature is proportional to the square of the applied voltage and inversely proportional to the thickness of the actuator to the third power. Furthermore, the curvature is expected to be independent of the actuator's length. Tests of actuators of three different lengths (73 mm, 110 mm, and 143 mm) generally agreed with the scaling relationship Eq. 1, as outlined in Fig. 1.6. However, they showed a minor dependence of the curvature on the actuator's length, likely due to higher-order effects not captured in our simplified analysis, such as out-of-plane deformation and edge effects. In these experiments, we achieved a maximum curvature of 12.5 $\pm$ 0.4 m^{-1} with a 73 mm long bimorph actuated at an initial electric field of 20 MV/m (10 kV applied to a 0.5 mm thick film).

A small modification of the simple scaling relationship detailed in Eq. 1 has im-

portant consequences for the design of the actuators. If the radius of curvature is large compared to the length of the actuator, i.e. $L/\rho \ll 1$, it can be shown that the transverse deflection δ of the actuator scales as

$$\delta \sim \frac{\nu \epsilon_0 \epsilon_r V^2 L^2}{E h^3} \ . \tag{5}$$

This basic scaling relationship describes the leading-order dependence of the actuator's motion on its geometry and applied voltage. It shows that the actuation depends on the length L and the thickness h, but considerably more strongly on the thickness. Hence in designs where it is desirable to maximize the deflection, efforts should be focused on reducing h rather than increasing L, keeping in mind that h too small would lead to dielectric breakdown and failure of the actuator. Designing around small h rather than large L has the added benefit of reducing the amount of material comprising the actuator, reducing costs and suggesting the potential for miniaturization.

Influence of water conductivity

The bimorph actuators were tested using water with a salt concentration comparable to that of seawater (35 g/L), deionized water, and United States Pharmacopeia (USP)-grade water (AquaPur, Decon) as both the internal and external fluids. We measured the conductivity of each of the three solutions and found them to be 48.15 $\pm$ 0.09, 0.045 $\pm$ 0.003, and 0.040 $\pm$ 0.002 mS/cm, respectively. To test the impact of water conductivity on actuator performance, we measured the maximum displacement of FEDEA bimorphs with matching internal and external fluids of either saltwater or USP-grade water, and found that the maximum actuation amplitude at 1 Hz was 2.0 and 1.7 mm, respectively Fig. 1.8. This demonstrates that that there is only a moderate impact of performance on the conductivity of the solution, and for reasons of simplicity we begin with deionized water as both the

internal and external fluid for the actuators in the robot but make no efforts to maintain the purity of the water. The time constant of a highly resistive ionic solution is greater than that of a more conductive solution, as described by Keplinger et al. [4]. However, it is still very small (on the order of 10^{-7} s), while the damping effects of the fluid viscosity and viscoelasticity of the elastomer [45, 46] have much slower timescales (order 10^{0}-10^{3} s) and thus dominate the time scale of the response, leading to a negligible difference in the observed performance of actuators in solutions with different ionic concentrations. One implication of this result is that the fluid electrodes are compatible in both freshwater and seawater environments.

Bioinspiration for swimming and transparency

Eels move quickly and efficiently using an undulating motion as a travelling wave traverses the body of the eel, known as anguilliform motion [47]. To produce anguilliform motion, we designed our swimming robot as three bimorph FEDEA modules placed end-to-end in series (Fig. 1.2). The robot is 22 cm long, 5 cm tall, and 1.5 mm thick. To imitate the travelling wave actuation observed in swimming eels, we actuated these six actuators in sequence (see Fig. 1.2, right). We connected each actuator to a power supply through a silicone tube filled with water, which terminates at a metallic syringe tip, providing electrical contact between the fluid chamber and the control electronics (Fig. 1.8). By controlling the sequence and timing of activation of the six actuators at a fixed voltage (7.5 kV), we generated an undulating motion in the robot (Fig. 1.2). To generate a propulsive travelling wave, inspired by the undulating motions found in eels, we actuated diagonal pairs of chambers in sequence from the anterior to posterior sections of the robot, as shown in Fig. 1.2.

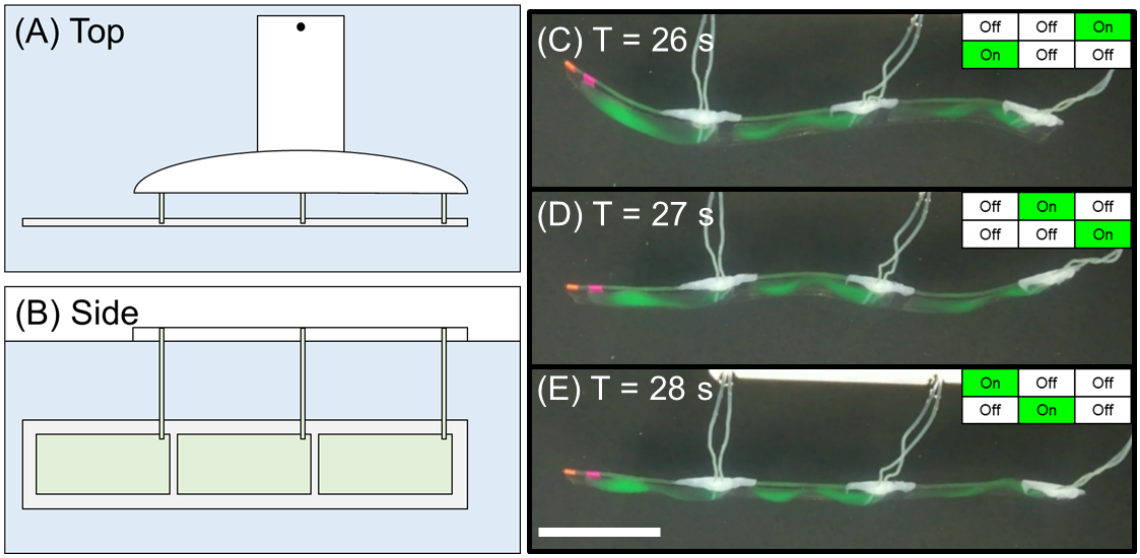

Figure 1.2: Schematic of experimental setup and screen captures from swimming. Top-down (A) and side (B) view schematics of experimental setup. The robot comprised three FEDEA bimorph modules arranged end-to-end. The motion of the swimmer was planarized by suspending it from a rotating boom by the tubing connected to each actuator. The boom permitted the robot to swim at a fixed depth in a large arc, reducing the impact of lateral tube tension on the robots performance. (C-E) Top-down view of actuator with time indicated. Inset diagram is a top-down schematic describing which of the six DEAs are at rest (Off) or actuated (On) in that frame. We cycled through the three states shown at a rate of 0.33 Hz, resulting in an average forward speed of 1.9 mm/s. The scale bar is 5 cm long.

Further, eel larvae, also known as *leptocephalus*, are translucent. Inspired by this, we designed our proof-of-concept swimming robot to be translucent. Since the internal electrode was a conductive fluid and the dielectric elastomer is a transparent membrane, the robot is transparent, with the exception of some residual hazing caused by the passivating agent used to pattern the electrodes (see Materials and Methods).

Swimming performance of the FEDEA

Since the FEDEA actuators consist of materials with densities that are comparable

to water, they face reduced buoyancy challenges found in pneumatically actuated fish-like soft robots [48]. To maintain a consistent swimming depth for performance characterization, we tuned the actuator to be negatively buoyant and suspended the actuator from a floating boom Fig. 1.2. The wetted areas of the actuator, tubing, and boom are 230, 23, and 270 cm^2, respectively. By sequential activation of the electrodes, we generated an undulating motion, enabling forward propulsion. We measured a maximum swimming speed of 1.9 mm/s (0.009 body lengths/s) at a driving frequency of 0.33 Hz. To better understand the performance of this proof-of-concept robot, we calculated the mean thrust and Froude propulsive efficiency η_{EBT}, based on Lighthill's elongated body theory (EBT) [47,49–51]. We found the parameters needed for calculating the thrust and Froude efficiency based on EBT (i.e. amplitude, wavelength, and wave speed) by fitting to experimental data of the position of the tail of the robot over time. We estimated the efficiency of the robot using Lighthill's elongated body theory as $\eta_{EBT} = 1 - \frac{V-U}{2V}$, where U is the mean swimming speed and V is the wave speed. For a driving frequency of 0.33 Hz, we measured a wave speed of 0.055 m/s, resulting in a η_{EBT} of 52%. The measured Froude efficiency informs us that excess effort is wasted in generating lateral motion in our robot; only approximately half of the effort is converted into useful thrust. One metric of swimming efficiency is the Strouhal number [52], which is proportional to the product of the tail-beat amplitude and driving frequency, and inversely proportional to the velocity. As a preliminary optimization of the swimming gait of the robot, we measured the amplitude as a function of driving frequency for an FEDEA bimorph (Fig. 1.10). From this, we observe a peak value of the product at a driving frequency of 0.5 Hz. When we increase the actuation frequency of the multi-segmented robot from 0.33 Hz to 0.5 Hz, we observe a 12% increase in average

swimming speed for the same actuation sequence. This demonstrates the opportunity for further optimization of the actuation sequence and frequency. For consistency, the results described in the remainder of the paper refer to the performance of the robot actuated at 0.33 Hz.

Power consumption during actuation

We calculated the electrical power input that the robot consumed to be 34 mW, based on the change in capacitance as $P_{electrical} = C_{act}V^2 f$, where C_{act} is the capacitance of the actuator when charged, V is the applied potential, and f is the driving frequency. The capacitance at rest was measured directly with an LCR meter, and the capacitance when actuated was calculated based on the deformation of the area and thickness of the robot based on Hooke's law and Pelrine's equation [2]. We also calculated the power consumption experimentally by measuring the voltage and current in a single actuator during a charge and discharge cycle and found the total power consumption for the robot (six actuators) to be $\sim$20 mW, which is comparable with the calculated value based on the change in capacitance. We calculated the mean thrust using EBT to be 0.25 mN over three tail beat cycles at a driving frequency of 0.33 Hz. We also measured the thrust experimentally and found a mean thrust of 42 ± 7 μN. Taking the lower of these two values, the mean power output based on the experimentally measured thrust was 0.08 μW and power density was 3.2 μW/kg for an actuator mass of 25.1 g. The power efficiency of the actuator, based on the mean thrust and electrical power input, ($\eta = P_{thrust}/P_{electrical}$) was 0.0013%. While the η_{EBT} describes the relationship between lateral motion and useful forward propulsion, the power efficiency here shows that approximately 0.0013% of electrical power used to deform the actuator results in thrust.

Acoustic profile demonstrating the sonic stealth potential of the robot

One advantage of using DEAs for underwater propulsion is the ability of our soft robot to move quietly, which is of considerable importance in stealth and acoustic monitoring applications. To demonstrate the quiet propulsion of our robot, we recorded the acoustic profile of FEDEA actuators in water at rest and during actuation and showed that there was only a slight increase in measured sound with an average value of 0.3 dB when the actuators were running (Fig. 1.11).

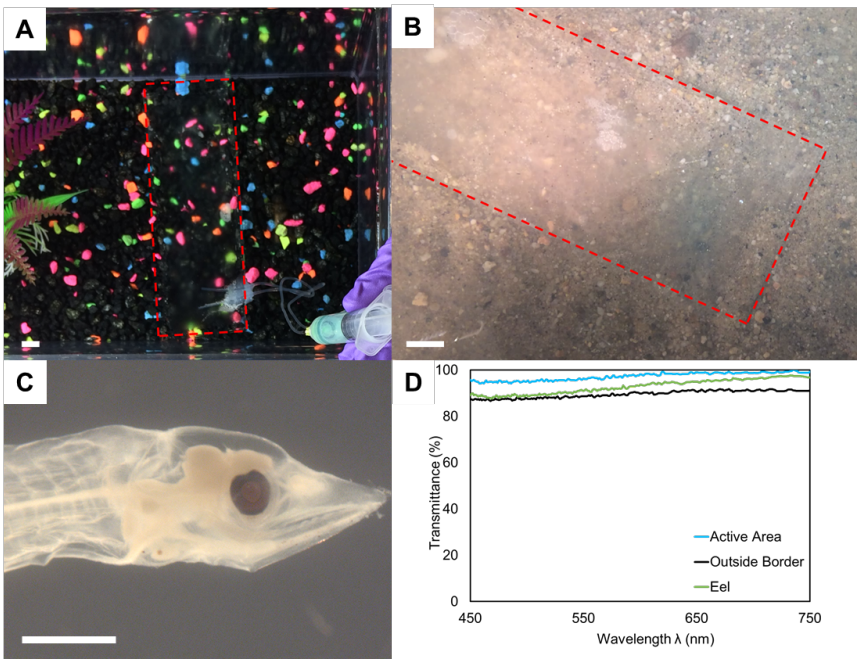

Figure 1.3: Demonstration of translucency. Photographs of the actuator over backgrounds of aquarium rocks (A) and sand (B), with dotted lines indicating the edge of the actuator. C) Microphotograph of leptocephalus (only head shown) from SIO Marine Vertebrate Collection, illustrating the high transparency of the eel. D) Transmission spectrum taken by hyperspectral imaging for two distinct regions in the actuator (active area, where the fluid electrodes are located, and the outside border) compared to the eel, demonstrating that the two sections of the actuator are in the range of transmittance values of the eel in the visible spectrum. Scales are 1 cm in A and B, 1 mm in C.

Translucency for optical camouflage

For applications where transparency or passive camouflage is desired, the robot should exhibit high transmittance throughout the visible spectrum (Fig. 1.3). To quantify the translucency, we measured light transmission through the actuator. There were two visibly distinct regions in the actuator–the border, which consisted of three layers of a transparent acrylic elastomer, and the active area, where the fluid electrodes resided. Using hyperspectral imaging [53, 54], we found that the active area had a transmittance of 97% compared to the border transmittance of 90%. The higher transmittance of the active area may be due to an improvement of light transmission through the water-elastomer interfaces in the area, which are diminished in the air-elastomer interfaces around the border. As a comparison, we measured the transmittance in the abdomen of a *leptocephalus* that uses translucency for camouflage [43]. We found that the transmittance of the two areas of the actuator were comparable to that of the eel, which had an average transmittance of 94% (Fig. 1.3).

Visual communication using fluorescence

In addition to passive camouflage, the high transmittance of the robot enables visual display through the body of the robot for communication. Recently, species of brightly fluorescent eels have been found in the Caribbean Sea [55]. While the purpose of the biofluorescence is still up for debate [56], one purpose may be to help eels locate each other during full moon spawning events. Other proposed functions may be to aid in communication, predator avoidance, or prey attraction. In robotic applications, fluorescence may be a way to enable communication optically in an environment that is not conducive to radio communication [57]. To test the feasibility of encapsulating a fluorescing dye

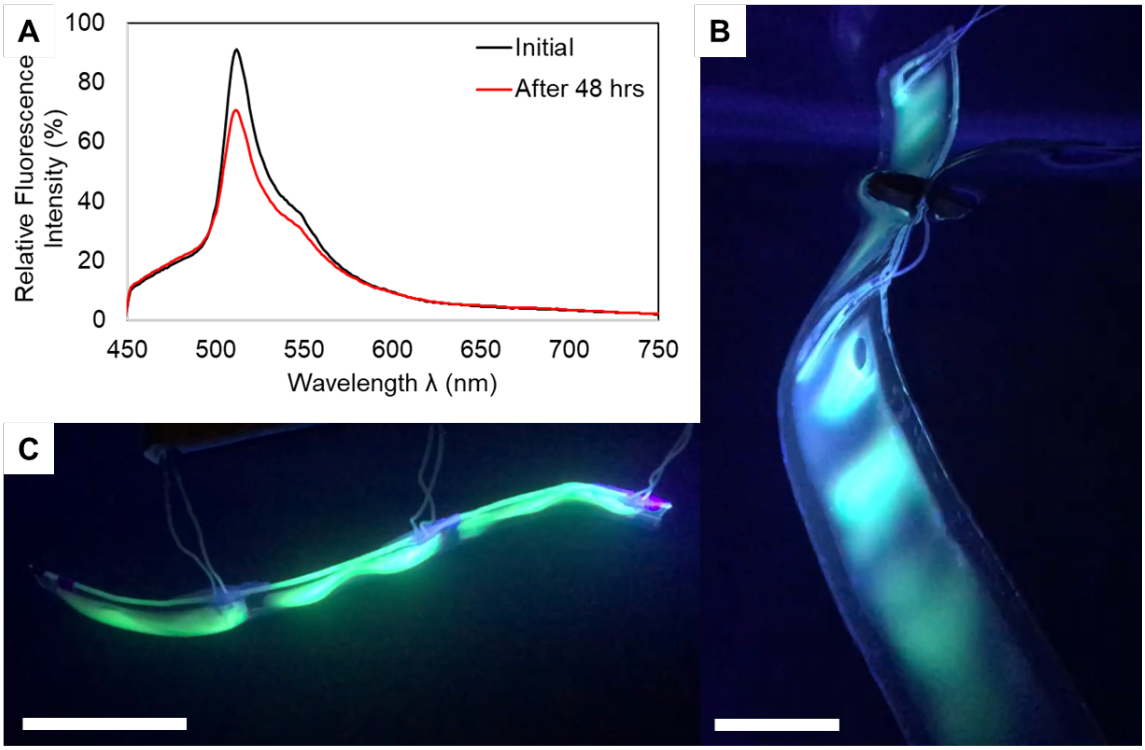

Figure 1.4: Fluorescence response of actuator. A) Emission spectrum (exc. 390 nm) of commercially purchased green fluorescence protein (GFP) embedded between two layers of VHB measured initially after injection of GFP and after 48 hrs of storage in the dark at room temperature. B and C) Photos of actuator fluorescing under UV/blue light stimulation. Scale is 5 cm.

within our actuators, we injected green fluorescent protein (GFP) between two layers of the dielectric film (in a similar configuration to the fluid electrodes described above) and plotted the initial and subsequent emission spectrum after two days of storage in the dark at room temperature (Fig. 1.4). These results showed that the fluorescence response of the GFP within the actuators did not decay significantly after 48 hours of encapsulation.

For larger volume testing, we then introduced a low-cost, non-GFP commercial

dye that fluoresces under UV excitation into the actuation chambers of our swimming robot. We then excited the dye with UV illumination while simultaneously actuating the robot (see Fig. 1.4). Taking advantage of the high transmittance of the actuator, we were able to use the entire internal electrode area for display, simultaneously maximizing the size of the DEA and the display.

Swimming performance calculations

The Froude efficiency was calculated as $\eta_{EBT} = 1 - \frac{V-U}{2V}$ where U is the mean swimming speed and V is the wave speed. The wave speed was calculated as the driving frequency (f) multiplied by the wavelength (λ), which were found by fitting the position of the tail of the actuator to $y = A\sin(c - b(t + t_{offset})) + v_{offset}$, where A is the amplitude and $t_{offset}$and v_{offset} are constants to align the model to the robot. The fitting parameters b and c are used to determine the frequency, wave speed, and wavelength, as $\mathrm{f} = \frac{b}{2\pi}$, $\mathrm{V} = \frac{\mathrm{b}\lambda}{2\pi}$, and $\lambda = \frac{2\pi \mathrm{l}}{\mathrm{c}}$, respectively, where l is the length of the actuator. We used the Curve Fitting Tool in MATLAB R2016a to fit the parameters to the data and include the fitting parameters and r^2 values in Table 1.1. We plot a representative comparison between the fitted model and experimental results in Fig. 1.9. We then used the fitted value of the wave speed to find the Froude efficiency, resulting in a Froude efficiency of 52% for a driving frequency of 0.33 Hz.

The mean thrust was found from Lighthill's EBT as $\mathrm{T} = \mathrm{mwW} - \frac{\mathrm{mw}^2}{2}\frac{\mathrm{dx}}{\mathrm{da}}$, where m is the virtual mass per unit length, w and W are the velocity of the tail perpendicular to the tip of the tail and perpendicular to the direction of motion, respectively, and $\frac{\mathrm{dx}}{\mathrm{da}}$ is the cosine of the angle between the tip of the tail and the mean swimming direction. To reduce errors attributed to measuring the experimental position of the tip of the tail over

time, we used the y position determined from the kinematic model. The virtual mass per unit length (m) was calculated as $\mathrm{m} = \frac{1}{4\pi \mathrm{s}^2 \rho}$, where s is the depth of the robot and ρ is the density of water. Measuring the position of the tip of the tail and the angle between the tip of the tail with respect to the direction of motion during swimming allows us to then calculate the mean thrust.

Experimental measurement of thrust

We measured the thrust experimentally by causing the boom to press against a strip of metal when the robot was swimming at steady state and used Euler-Bernoulli beam theory to calculate the thrust of the robot based on the deflection in the beam. The beam was a 1 cm tall, 5 cm long, and 50.8 μm thick strip of spring steel with a Young's modulus of 201x10^9 Pa. We measured the deflection of the tip of the beam and found an average deflection of 79 μm, corresponding to a mean thrust of 42 $\pm$ 7 μN.

Longevity study

We submerged FEDEA bimorphs with USP-grade electrodes and measured the amplitude as a function of time at a driving frequency of 1 Hz. The silicone tubing and sealant were raised above the water level to eliminate their effects on the longevity of the DE. We measured the dynamic response of the actuator when it was first made, after 100,000 cycles, and after 1,000,000 cycles, corresponding to 0, $\sim$100, and $\sim$300 hours of continuous immersion in water. We measured an average amplitude over three actuation cycles of approximately 5 mm in each case, although this experiment was not significantly precise to detect small changes in the amplitude of actuation. Nonetheless, this result demonstrates that the actuators can be operated over 300 hours of continuous immersion and 1 M cycles with little change in their overall performance. However, when the robots

are fully submerged, we have noticed that they typically fail after 10^2 to 10^3 cycles, due to challenges with sealing around the tubing. These results suggest that further optimization of the fabrication approach may enable robots with lifetimes of over 1 M cycles.

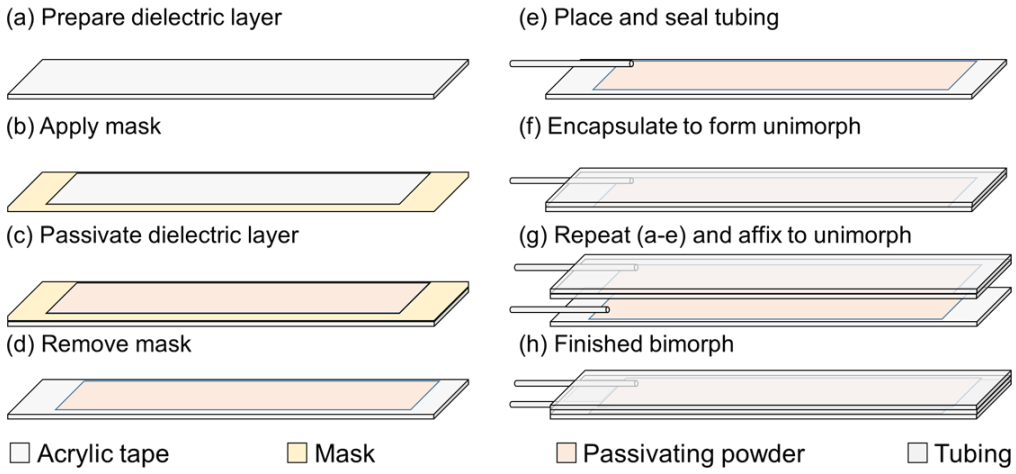

Figure 1.5: Fabrication process for bi-directional fluid electrode DEA. The actuator was fabricated in eight steps: (a) Preparation of the first acrylic adhesive layer; (b) addition of a mask patterned using a laser machining system; (c) application of a passivating layer to define the active area; (d) removal of the mask; (e) placement tubing for fluid and electrical connections and seal around tubing with silicone sealant, repeating steps (a-e) for bimorphs; (f) encapsulation with an additional acrylic adhesive layer, resulting in a unimorph fluid electrode DEA; (g) application of unimorph to second partial structure created in step (e); and (h) resulting bimorph structure.

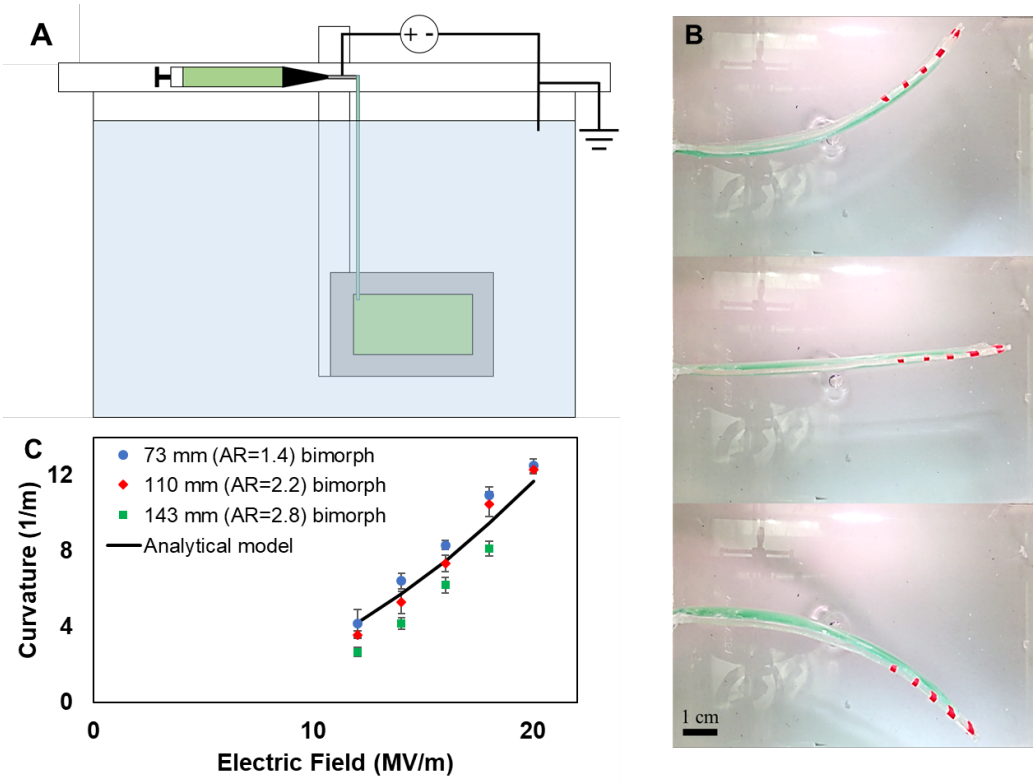

Figure 1.6: Bimorph experimental setup, images, and results. A) We supplied power to the actuators by clamping the high voltage lead of the power supply to the metal tip of the syringe, which was in contact with the fluid electrode. We affixed the actuator to a vertical acrylic beam during actuation to simplify measurements. We grounded the bath via a submerged wire connected to Earth ground. We include representative images from bending experiments in (B). The middle image corresponds to when there was no applied voltage to either fluid chamber. The top and bottom images were taken three seconds after 8 kV was applied to the lower and upper fluid chambers, respectively. We plotted the curvature (C) as a function of applied voltage for three different lengths of actuators. The error bars are the standard deviation and N=3 for all measurements.

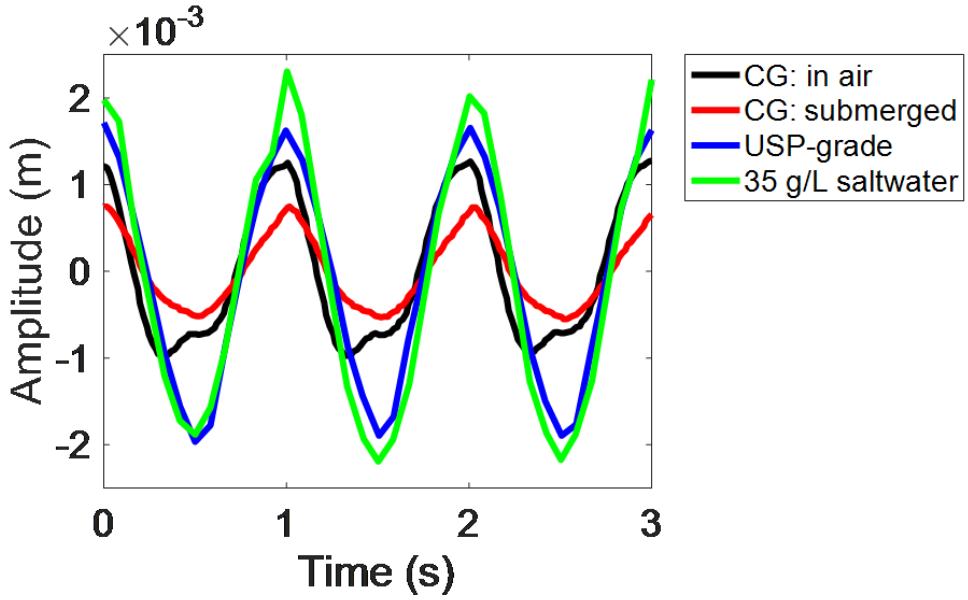

Figure 1.7: Performance comparison of carbon grease and FEDEA bimorphs. We prepared prestrain-free bimorph actuators with carbon grease electrodes, USP-grade water, and saltwater as the internal electrodes. The actuator is driven at 1 Hz and we plot the amplitude as a function of time for the actuator in air and submerged in water.

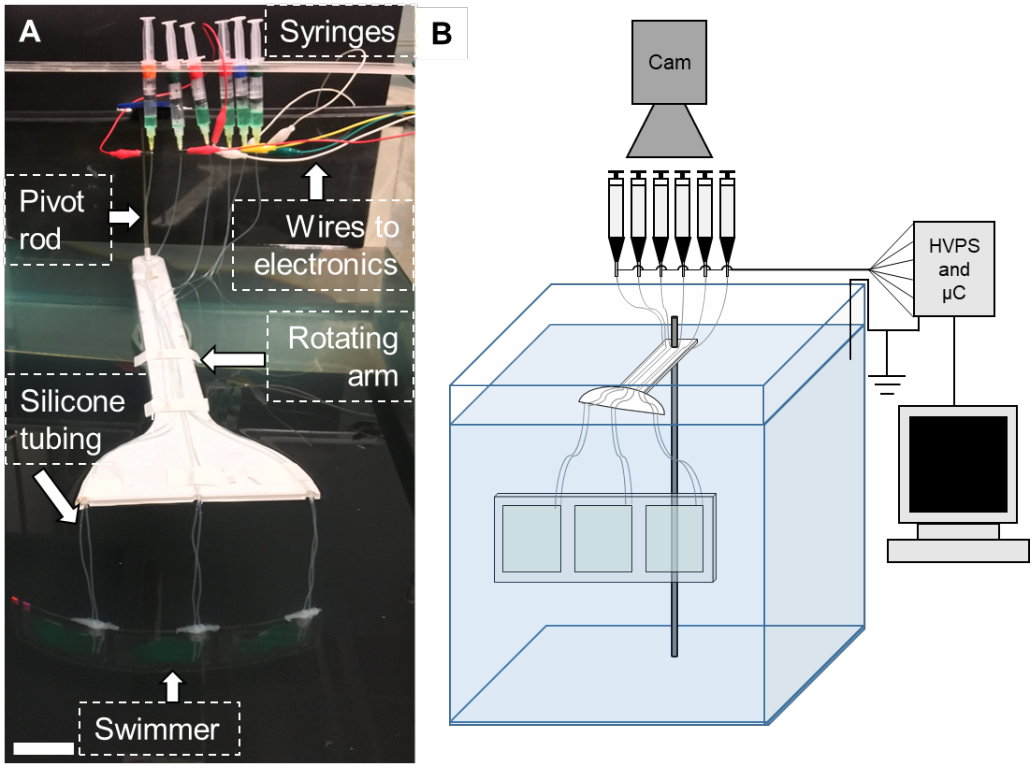

Figure 1.8: Photograph and schematic of experimental setup. A) We suspended the robot from its tubing which we attached to a floating, rotating boom that is free to pivot around a rod. The rotating boom planarizes the motion of the robot while minimizing the effects of lateral tension from the tubing during swimming. We connected each tube to a syringe which we used to inject fluid into each actuator and provide electrical connection between the electronics and robot. B) Corresponding schematic illustrating the various components of the experimental setup. Scale is 5 cm.

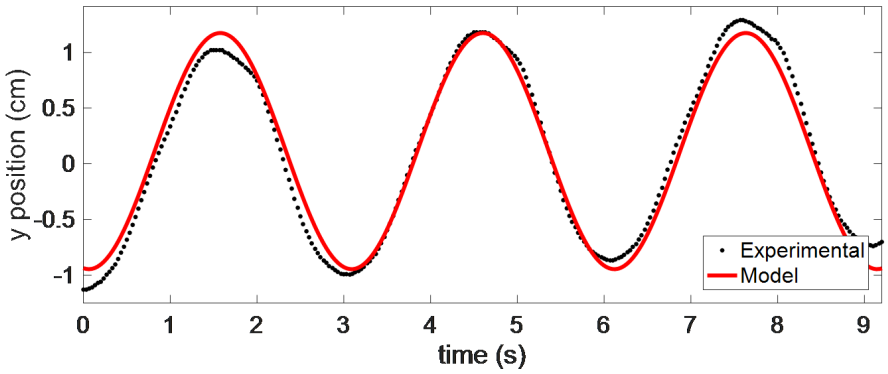

Figure 1.9: Comparison of experimental data and kinematic model. Position of the tip of the tail over three cycles for a driving frequency of 0.33 Hz with the analytical model plotted for comparison. Fitting parameters are described in Table S1.

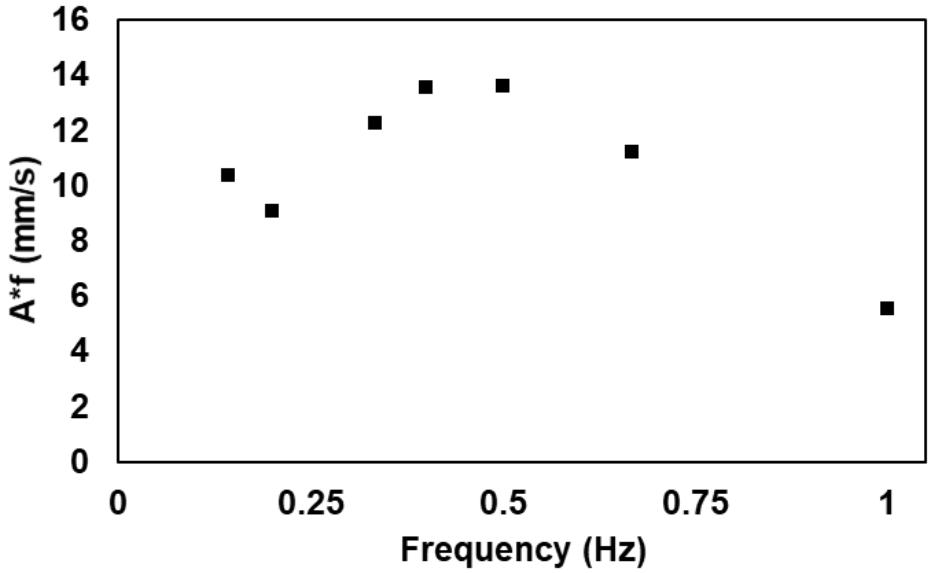

Figure 1.10: Effect of actuation frequency for a bimorph FEDEA underwater. For a 143 mm long bimorph FEDEA, we measured the amplitude of actuation as a function of driving frequency and plot the product of amplitude and frequency as a function of frequency. The maximum value is found at a frequency of 0.5 Hz.

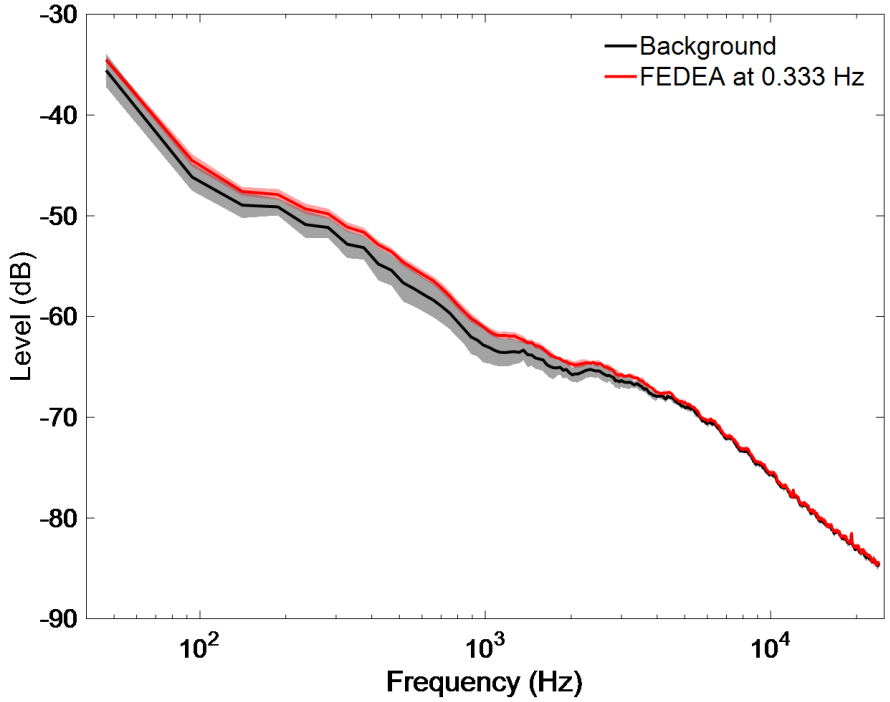

Figure 1.11: Sound intensity results. We placed a hydrophone at ∼5 cm from an FEDEA bimorph and recorded the sound both when the actuator was off (background) and when we actuated it at 0.33 Hz. We plot the average spectrum (solid line) and standard deviation (shaded region) for three trials of both cases, showing that there was only a slight increase in the measured sound level between 40 Hz and 24 kHz, with an average difference of 0.3 dB.

Table 1.1: Fitting parameters for sinusoid kinematic model of the tail.

A (m)	**λ (m)**	**V (m/s)**	**t_{offset} (s)**	**y_{offset} (m)**	**r^2**
0.0106	0.1664	0.05496	1.633	0.001138	98%

DISCUSSION

The proof-of-concept design here demonstrates that water, including the surrounding fluid in submerged devices, can be used as compliant electrodes for DEAs. This design approach obviates the need for the use of hydrogel-, carbon-, or metal-based electrodes

and potentially simplifies the design of actuators for submersible robots which can take advantage of the ground potential provided by the surrounding fluid. The results in Fig. 1.7 show FEDEAs can provide greater actuation amplitudes than non-prestrained actuators with carbon grease. When a bimorph with carbon grease electrodes is submerged in water, the maximum amplitude decreases by 46%. However, the amplitude is $\sim$two times larger for FEDEAs with USP-grade water compared to submerged carbon grease electrodes. This demonstrates that the actuation performance decreases when the actuators are submerged in water, but fluid electrodes provide comparable, if not improved, actuation performance over carbon grease electrodes when submerged.

One advantage of compliant actuators and soft robotics in general is the ability to minimize the risk of damage to their surroundings, especially when interacting with living creatures, unstructured environments, or delicate objects [58–61]. The prototype robot presented here consists of completely soft, submersible actuators that take advantage of the conductivity and potential of its surrounding environment. Further, since the actuator is completely soft, it reduces the risk of harming wildlife or fragile structures in the case of contact between the robot and its environment. While non-polar liquids are known for causing swelling of the elastomer, polar liquids, including water, are regarded as being chemically stable with elastomers [36, 37] and minimize the risk of swelling.

One challenge with the current design is that the structure has a preferential direction of bending, resulting in asymmetric actuation about the midline of the robot. We believe that this is due to a slight curvature in the robot caused by our manufacturing approach which imparts a preferential bending direction in the actuators resulting in larger bending in one direction as shown in Fig. 1.2. Furthermore, the bi-directional expansion

of the actuated bimorph sections causes curvature in two direction that seems to inhibit bi-directional bending of the segments A conceptual constraint of fluid electrodes is that they are not amenable to all actuator configurations, in that one of the electrodes generally requires some encapsulation to define its geometry and ensure its contact with the DE membrane. The design and fabrication approaches described in this work also have a few additional design constraints: 1) the border around the electrodes need to be at least $\sim$8 mm wide to ensure adhesion and reduce the risk of shorting, 2) tubing is required to inject the fluid and maintain electrical contact, which must be free of air bubbles, and 3) a sealant is required to prevent leakage around the tubing/elastomer interface. One potential way to address these challenges, and potentially scale to smaller dimensions, is to use soft lithography, as used previously for DEA pumps [62, 63]. The actuator itself is neutrally buoyant, which reduces the need to overcome the negative buoyancy found in most, traditional underwater robotic systems. It is possible to fine-tune the buoyancy by introducing air into the fluid chambers or by ballasting to achieve negative buoyancy. The speed of our robot is slower than most reported underwater swimmers using smart actuators [64, 65], but previous swimmers based on DEAs are either opaque (due to electrode materials) or require prestrained dielectric membranes, or both. The boom serves to planarize the motion of the robot so that we can better characterize its performance. However, the boom also increases the drag resisting the motion of the robot. Since the robot is operating in laminar flow (Reynolds number of $\sim$450), it experiences viscous drag proportional to the combined wetted area of the robot, tubing, and boom. The actuator comprises 44% of the wetted area of the setup, indicating that the performance described here is a conservative estimate of the potential performance of the robot. Without this increased drag, we

estimate the steady-state velocity of the robot to be v' = 1/0.44x1.9 mm/s = 4.3 mm/s. The efficiency of our robot is less than the estimated η_{EBT} of swimming eels, which has been reported to range from 87% to 97% [51], however, the proof-of-concept actuation sequence presented here has not been optimized for speed or efficiency. One way to estimate the potential optimized performance of the robot is through EBT. If we were able to improve our robot such that it matched the efficiency of natural eels at a fixed body wave speed (e.g., by optimizing the parameters of the EBT model, nominally the amplitude at the tail, A, the amplitude growth rate, α, the length of the eel, L, and the wavelength of the actuation, λ) [66], then EBT predicts then we could expect a maximum speed of 55 mm/s.

As another point of comparison, the power efficiency of a commercially available remotely operated vehicle (ROV), the Trident by OpenROV, is estimated to be 15% [67, 68]. The Trident ROV has a maximum speed of 2 m/s and run time of 3-4 hrs on a 389 kJ battery that weighs 0.57 kg, resulting in a range of 22 to 29 km [67]. While the FEDEAs of our robot required very little power to generate thrust, the driving electronics consumed a comparatively large amount of energy. Our prototype circuit, which was not optimized for efficiency, consumed approximately 1 W during actuation, primarily due to discharging the DEAs through resistors. Since the robot reached an average speed of 1.9 mm/s, it is possible to estimate that if we powered it with a 389 kJ battery (without affecting the hydrodynamic drag) our robot would have an estimated range of $\sim$0.7 km.

While the speeds and efficiencies of the DEAs reported in (10, 11, 19) are much higher than those described in this work, we have done so without any prestrain, eliminating the need for rigid or semi-rigid members to maintain a stretch. This results in a fully soft elastomeric robot. For example, the speed and efficiency of the work by Li et al. are

71 and 7900 times greater than that of our robot, respectively [12]. However, their work does not perform as well on camouflage and conformability. While the submerged robots have a longevity of 10^2-10^3 cycles, we have observed that the elastomer membranes themselves can withstand over 10^6 actuation cycles and $\sim$300 hours of continuous immersion in fluid. Further improvements to the efficiency, range, and longevity of the robot are left for future work.

Since the robot is driven by DEAs, its propulsion system is silent, especially compared to propeller or jet thrusters used on typical ROVs. Optical transparency enables passive camouflage so that the robot can blend into its environment, and the combination of optical and acoustic stealth suggest the potential for underwater applications where detection or disturbance of the environment is undesirable. Recent work has explored electroluminescence in translucent soft robotics [69], which could be implemented in our swimming robot, enabling a more controllable, programmable display. We can implement optical communication through fluorescence, electroluminescence, or other techniques to enable alternative means of localization or communication underwater [70]. A fully contained soft robot driven by these fluid electrode DEAs could house miniature HVDC convertors, a microcontroller, cameras, sensors, and battery, which could be encapsulated in a watertight chamber that is electrically isolated from the surrounding fluid, as previously demonstrated for pre-strained DEA swimmers [12]. This would enable quiet, untethered, submersible, passively camouflaged soft robotics for search-and-rescue or ocean discovery operations.

MATERIALS AND METHODS

Actuator fabrication

To construct the bimorph actuator module, we attached two layers of an acrylic adhesive (VHB 4905, 3M) to each other (Fig. 1.5). We patterned the electrode chambers with a passivating agent (corn starch for bimorph characterization, superfine granulated sugar and dishwashing liquid for transparency and swimming experiments) to prevent adhesion between the layers in these regions. We inserted a silicone tube to enable the injection of a conductive fluid into the electrode chamber via a syringe. We used water as the conductive ionic solution and we added food dye to the internal conductive solution as a visual aid for the bimorph and some swimming experiments. The water that fills the actuators and the tank for swimming experiments was initially deionized, but we made no efforts to protect the purity of the water in the tank.

Characterization of actuation and swimming

We connected the fluid to a high voltage power supply through the metallic needle of the syringe, which provided electrical contact to the fluid within the actuator. A high voltage power supply (ES20P-5W, Gamma High Voltage Research, Inc.) provided the power for the bimorph actuator module curvature measurements. EMCO high voltage DC converters amplified the signal from a microcontroller (Arduino Uno) for the swimming experiments. We used a camera phone to record images and video in all experiments. We used the open source Tracker Video Analysis Tool (physlets.org/tracker) for motion tracking of the robot.

Fluorescence response

We used "Green UV Laser Dye" (Bitspower) as the dye and an LED flashlight (TaoTronics, excitation spectrum 395-400 nm) as a UV source in the fluorescing swimming experiments. We used a hyperspectral imaging system (PARISS® hyperspectral

imager, LightForm Inc.) mounted on a Nikon Eclipse 80i microscope to measure the fluorescence spectrum from commercially sourced GFP embedded between layers of the dielectric elastomer in the longevity study. We plot the spectra from 450 nm to 750 nm for evaluation of the longevity of the emission of the embedded within the GFP both initially after embedding the GFP and 48 hours later.

Translucency study

We measured the transmission of regions of interest in the robot and the *leptocephalus* with the PARISS hyperspectral imaging system. We selected two regions in the robot (around the outside border of the robot and over the active area) and one region in the *leptocephalus* to compare their transmission between 400 and 800 nm.

Acoustic measurements

To measure the acoustic profile of the robot, we used a hydrophone (Teledyne Reson) approximately 5 cm away from bimorph FEDEAs within a $\sim$700 mL water tank. We measured the sound both when the actuators were sitting at rest for a background signal and when we actuated the bimorphs at 0.33 Hz. We recorded the signal with a Sound Devices 722 high resolution digital audio recorder and analyzed the spectrum with Audacity using a Hanning window and a size of 1024.

Conductivity measurements

Data was obtained using a potentiostat (PalmSens 4, Enschede, Holland), on a 3-electrode system consisting in 4 mm diameter gold working, gold counter, and Ag/AgCl reference electrodes (DRP-220AT, Dropsens, Oviedo, Spain). Impedance measurements at 0 V *vs.* Ag/AgCl, 0.01 mV AC in frequencies from 5 Hz to 100,000 Hz. Conductivity of the solution was calculated using the following equation $\kappa = \frac{A}{Z\,l}$, where κ is the con-

ductivity of the solution, A is the area of the electrode, Z is the impedance at 100 kHz, and l is the length between electrodes.

ACKNOWLEDGMENTS

The authors would like to acknowledge the advice and assistance of Michael C. Allen (Marine Biology Research Division (MBRD), Scripps Institution of Oceanography (SIO)) in performing the translucency and fluorescence experiments, and Dr. Maya de Vries (MBRD, SIO, and UC San Diego) for acoustic measurements. We also thank Benjamin Frable for providing samples of leptocephalus larvae from the SIO Marine Vertebrate Collection, which were used for optical, hyperspectral, and imaging analyses. We also thank Dr. Ada Martn Galn for assistance with the conductivity measurements. Funding: This work is supported by the Office of Naval Research grant number N000141712062. C. Christianson is supported by National Science Foundation Graduate Research Fellowship grant number DGE-1144086. D.D.D. acknowledges financial support from the Lounsbery Foundation. Author contributions: C.C., N.N.G., M.T.T. conceived of the project, designed the prototypes and experiments, and analyzed the data. C.C. and N.N.G. fabricated prototypes and conducted experiments. D.D.D. conceived, designed, conducted, and analyzed translucency and fluorescence experiments. N.N.G and S.C. developed the analytical models. All authors contributed to, and agree with, the content of the final version of the manuscript. Competing interests: The authors declare no competing interests. Data and materials availability: Data is available from the authors upon request.

Chapter 1, in full, is a reprint of the material as it appears in Science Robotics, 2018. Christianson, Caleb; Goldberg, Nathaniel N.; Deheyn, Dimitri D.; Cai, Shengqiang;

Tolley, Michael T., Science 2018. The dissertation author was the primary investigator and author of this paper.

Chapter 2

Jellyfish-inspired Robot Driven by FEDORAs

Caleb Christianson[1], Christopher Bayag[2], Guorui Li[3], Saurabh Jadhav[2], Ayush Giri[4], Chibuike Agba[4], Tiefeng Li[3], and Michael T. Tolley[2,*]

[1]Department of Nanoengineering, UC San Diego, La Jolla, CA 92093

[2]Mechanical and Aerospace Engineering, UC San Diego, La Jolla, CA 92093

[3]Institute of Applied Mechanics, Zhejiang University, Hangzhou, China 310013

[4]Department of Mechanical Engineering, Howard University, Washington, DC 20059

Abstract

Robots for underwater exploration are typically comprised of rigid materials and driven by propellers or jet thrusters, which consume a significant amount of power. Large power consumption necessitates a sizeable battery, which limits the ability to design a small robot. Propellers and jet thrusters generate considerable noise and vibration, which

is counterproductive when studying acoustic signals or studying timid species. Bioinspired soft robots provide an approach for underwater exploration in which the robots are comprised of compliant materials that can better adapt to uncertain environments and take advantage of design elements that have been optimized in nature. In previous work, we demonstrated that frameless DEAs could use fluid electrodes to apply a voltage to the film and that effective locomotion in an eel-inspired robot could be achieved without the need for a rigid frame. However, the robot required an off-board power supply and a non-trivial control signal to achieve propulsion. To develop an untethered soft swimming robot powered by DEAs, we drew inspiration from the jellyfish and attached a ring of frameless DEAs to an inextensible layer to generate a unimorph structure that curves towards the passive side to generate power stroke, and efficiently recovers the original configuration as the robot coasts. This swimming strategy simplified the control system and allowed us to develop a soft robot capable of untethered swimming at an average speed of 3.2 mm/s and a cost of transport of 2.8. This work demonstrates the feasibility of using DEAs with fluid electrodes for low power, silent operation in underwater environments.

INTRODUCTION

Robots are being used in increasing numbers for underwater exploration and environmental monitoring [71] and will continue to serve as a valuable data collection tool for scientists [72]. However, traditional robots introduce their own risks. Since robots are typically made from rigid materials that can move quickly, they pose inherent danger when operating near fragile structures and creatures and may become lodged in confined spaces. Additionally, underwater robots are usually driven by propellers or jet thrusters, which generate considerable noise and vibration. This additional noise is especially prob-

lematic when studying elusive animals or when studying underwater acoustics. Lastly, they consume a large amount of power, requiring considerable batteries or a tether. Recent work by Jaffe et al. demonstrated the deployment of low power profiling floats to study the conditions of large regions of the ocean as they change over time [73], however the floats only have a buoyancy control and aren't capable of lateral swimming.

The growing field of soft robotics presents a promising approach to designing robots that make them more adaptable to their environments [14, 25, 43, 74], facilitating safer interactions with fragile objects and creatures, and can enable silent, low power locomotion [12, 75]. Many soft robots are driven either pneumatically or hydraulically by pressurizing and depressurizing fluidic actuators to generate propulsion [48, 76, 77]. However, soft robots powered by fluidic actuators require bulky, rigid pumps that consume considerable power.

In this work, we developed a low power, silent, soft, jellyfish-inspired robot driven by fluid electrode dielectric organic robotic actuators (FEDORAs). We used a mechanical model to determine optimal dimensions and validated it with experimental data. Considering fluid dynamic analyses of jellyfish locomotion, we hypothesized that the system would have an optimal driving frequency that maximizes speed and minimizes COT, which we confirmed experimentally. To enable untethered propulsion, we designed a waterproof, untethered power supply for driving the robot. These efforts resulted in a silent, low-power, untethered soft swimming robot capable of jellyfish-inspired locomotion, comprised of actuators with a maximum deflection of 10 mm, maximum force of 6.1 mN, and maximum work output of 16 μJ. A tethered version swims at a maximum speed of 1.8 mm/s and a cost of transport (COT) of 21. The untethered robot achieved an average speed of

3.2 mm/s with a COT of 2.8. The layout of the rest of the paper is as follows: in section 2 we give an overview of jellyfish locomotion, previous work on jellyfish-inspired robots, and dielectric elastomer actuators; section 3 describes the design of our robot; section 4 discusses our experimental design; in section 5 we provide our results; and we end with a discussion of the work and our conclusions.

BACKGROUND

Jellyfish locomotion

The jellyfish is the most efficient ocean swimmer, in terms of cost of transport which relates the energy required to move a unit mass a unit distance [78]. Jellyfish have a thin layer of muscles on the underside of their bell, which they contract to eject a volume of fluid from within their bell. The ejected fluid propels the jellyfish forward. The jellyfish then releases the contraction on their muscles and the elasticity of the jellyfish restores the bell to its initial volume. In other words, the jellyfish primarily expends energy during the contraction phase in which energy not transferred to the fluid can be stored in the elastic structure, and the stored energy can be recovered during the relaxation phase of their swimming cycle. This approach of passive relaxation enables the jellyfish to achieve such high efficiency. Jellyfish swim the fastest and the most efficiently at or near their resonant frequency, based on the stiffness and dimensions of their bell [79]. The pulse frequency that jellyfish swim at is also inversely proportional to their mass and reduce their pulse frequency as they grow to avoid a high energetic cost of driving a large mass at a high frequency [80].

Actuation for jellyfish-inspired robots

Recently, an untethered jellyfish-inspired soft robot was developed using hydraulic

actuators [81]. One challenge with fluidic actuators is that they necessitate either a pump or piston for pressurizing the chambers, which often draw a considerable amount of power and are made from rigid materials. Nawroth et al. presented a tissue-engineered jellyfish-inspired robot that used cardiac myocytes (heart cells) for actuation [82]. This approach resulted in a completely soft, jellyfish-inspired robot, but contained myriad fabrication and storage challenges commensurate with implementing biological tissues into a robotic actuator. Several jellyfish-inspired robots have been developed with with actuators based on shape memory alloys (SMAs) [83, 84]and ionic polymer-metal composites (IPMCs) [85]. Ren et al. developed a small scale soft robot that employed an external field to actuate magnetic lappets [86]. Their work demonstrated the ability to effectively swim and transport cargo, but required an external field for propulsion. Recently, Cheng et al. demonstrated an untethered soft robotic jellyfish that was powered by dielectric elastomer actuators (DEAs) that swam with a maximum speed of 1 cm s^{-1} [87].

Overview of DEAs

DEAs provide an energy efficient method of achieving deformations with high strains for soft robots [2]. Recent efforts on jellyfish-inspired robots driven by dielectric elastomer actuators include that by Godaba et al. in which they developed a pressurized DEA membrane that expanded to eject a volume of water from within a 3D printed shell [28], and a soft, multi-lobed flapping robot developed by Shintake et al. [13]. DEAs are a type of smart material consisting of a dielectric polymer membrane with two conductive electrodes on either side [3]. A high voltage is applied through the electrodes across the membrane. As charges accumulate on either side of the membrane, attraction of opposite charges compresses the film in thickness while repulsion of like charges on the surfaces

expands the film in area. If the actuator is laminated to a flexible but inextensible strain-limiting layer, the actuator will curve towards the inextensible layer as it lengthens. One of the benefits of DEAs is that they are energy efficient and have a reported electromechanical conversion efficiency of 90% [2]. Energy loss occurs through current leakage through the dielectric as well as viscoelastic losses from the material [88]. Practically, additional energy is lost when the actuators are discharged, as the accumulated charges are typically shunted to ground through a resistor.

The dielectric film in a DEA is typically either a silicone or acrylic based elastomer (e.g., polydimethylsiloxane—PDMS—or the acrylic adhesive VHB from 3M). The compliant, conductive electrodes can be made from a variety of materials, including thin films of deposited metals; conductive hydrogels; or carbon-based electrodes that are either in a dry powder form, suspended in a silicone grease, or dispersed in an elastomeric matrix. Deposited metals feature high conductivity but their stiffness precludes them from most practical DEA applications and they typically require a deposition in a cleanroom environment or other costly fabrication approaches. Conductive hydrogels are transparent, conductive, and compliant, but they need to be encapsulated to avoid dehydration, impart some non-negligible stiffness, and require some effort to fabricate [4, 12]. Carbon-based electrodes are the most widely used materials for compliant electrodes in DEAs due to their low cost, high compliance, and ease of prototyping, but also need to be encapsulated to prevent smearing under mechanical abrasion. The silicone oil in carbon grease is also reported to disperse through the dielectric membrane, affecting the properties and lifetime of the actuators.

We recently reported that water makes an excellent conductive electrode, espe-

cially for underwater applications [42, 62, 75]. Five key advantages of using water for compliant electrodes in a DEA are that fluid electrodes 1) impart no additional stiffness to the structure and are fully compliant to deformations of the actuator; 2) eliminate the need for an external encapsulation layer, reducing the overall stiffness and complexity of fabrication; 3) can be transparent; 4) are inexpensive and straightforward to manufacture; and 5) can be loaded with dyes or other solutions for visual communication or other applications. Previously, we developed an eel-inspired swimming robot that used a series of bimorph fluid electrode dielectric organic robotic actuators (FEDORAs) to undulate through the water at a maximum speed of 1.9 mm/s [75]. In addition, while many DEAs rely upon being prestrained and having a rigid or semi-rigid frame to maintain that strain, prestrained actuators demonstrate a number of disadvantages, including the need to use a rigid frame, the challenge of rupturing the film during prestrain, and the impractability during many applications, especially in soft robotics where compliance is advantageous [89].

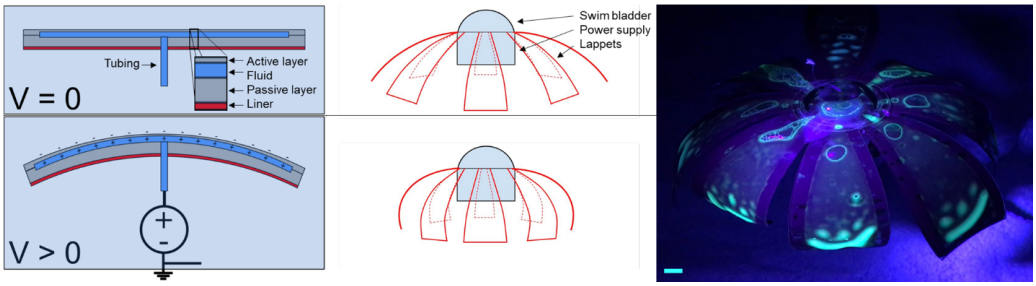

Figure 2.1: Working principle and fluorescence image of the jellyfish-inspired robot. Left: working principle of FEDORAs. The FEDORAs comprise two elastomeric layers that encapsulate a conductive fluid. We attach an inextensible layer to the underside of the actuator as a strain-limiting layer. We insert a silicone tube that serves as a conduit for the conductive fluid and connects the internal fluid electrode to the high voltage power supply. When we apply a voltage to the internal fluid electrode w.r.t. the surrounding fluid, Maxwell forces induce a pressure on the dielectric membrane, causing it to lengthen and thin, which results in bending towards the inextensible layer. Center: to achieve untethered swimming, we designed an axisymmetric array of FEDORAs and attached a waterproof high voltage power supply. A swim bladder provides buoyancy control. When the power supply is on, the electrostatic forces cause the lappets of the robot to bend downward, generating a net thrust upwards. Right: Screen captures, in which we demonstrate the transparency of the dielectric membrane and fluid electrodes by adding a fluorescent dye to the fluid which we stimulate with an ultraviolet light. Scale bar is 1 cm.

Robot design

Description of overall design

The overall design is based on an axisymmetric array of unimorph actuators, as shown in Figure 2.1. The outer surface of the robot is an active dielectric elastomer actuator, which expands in area when we apply a voltage to it. To apply the voltage, we implement fluid electrodes—one electrode is a thin film of fluid that is encapsulated underneath the dielectric elastomer, and the other electrode is provided by the surrounding, grounded fluid that the robot is immersed in. A second layer of dielectric elastomer encapsulates the inner fluid electrode. A flexible but inextensible film serves as a strain-limiting

layer and provides a small prestrain to the dielectric elastomer. We establish electric contact between the inner fluid electrode and a power supply through a silicone tube with a fluid that provides a conducting path. When we apply a voltage through the fluid across the dielectric elastomer, the elastomer expands in area and the bell of the jellyfish-inspired robot contracts. This contraction accelerates fluid around the edge of the bell, enabling forward propulsion of the robot.

Design of the unimorph actuators

Each actuator comprises four layers—the active dielectric elastomer, the fluid electrode, the passive dielectric elastomer, and the strain-limiting layer, as shown in Figure 2.1. To determine an optimal selection of thicknesses and modulus for each of these layers, we employed an analytical mechanical model [90]. We used the model to calculate the expected deflection, blocked force, and work while varying the applied voltage to the active layer and the thicknesses of each of the layers. Under no load, the curvature of a bilayer structure is defined by the well-known Timoshenko equation. For maximum deflection, the structure should be as close to a simple bilayer as possible where the thickness and modulus of layers are matched. However, to generate high force, thicker layers are required. This is the conflicting relationship between achieving both high force and large deflections. To develop effective actuators for underwater propulsion, we investigated configurations that would maximize work. There are also practical reasons to avoid a simple bilayer structure—charges would accumulate and impart electrostatic forces on both layers of the actuator.

We selected the dielectric elastomer layers to maximize the strain they could generate based on commercially available materials and electronic components. We chose an

acrylic-based elastomer for the dielectric layers due to its high actuation response, self-adhesion, and prevalence in DEA research which improves its ability to be compared with existing work and to be used by other researchers. We have found four thicknesses for commercially available acrylic elastomers and selected the one that would provide the largest strain at the maximum voltage that we could achieve with a commercially available high voltage power supply without suffering breakdown. We used the analytical mechanical model to determine the optimal thickness of the passive dielectric layer that would maximize work. While a passive layer that matches the thickness of the active layer should achieve the highest deflection, a thicker passive will provide greater force. Thus, we need to select the thickness that will provide the greatest total work. We also used the model to predict the increase in work that could be achieved by an additional, stiffer, strain-limiting layer.

Additionally, DEAs are known to have improved performance when they are prestrained, however, prestrained DEAs typically require a rigid frame to maintain that strain. Alternatively, we imparted the strain-limiting layer with some initial curvature to apply a prestrain to the DEAs. This layer provides a small initial prestrain to the actuators, which increases their performance.

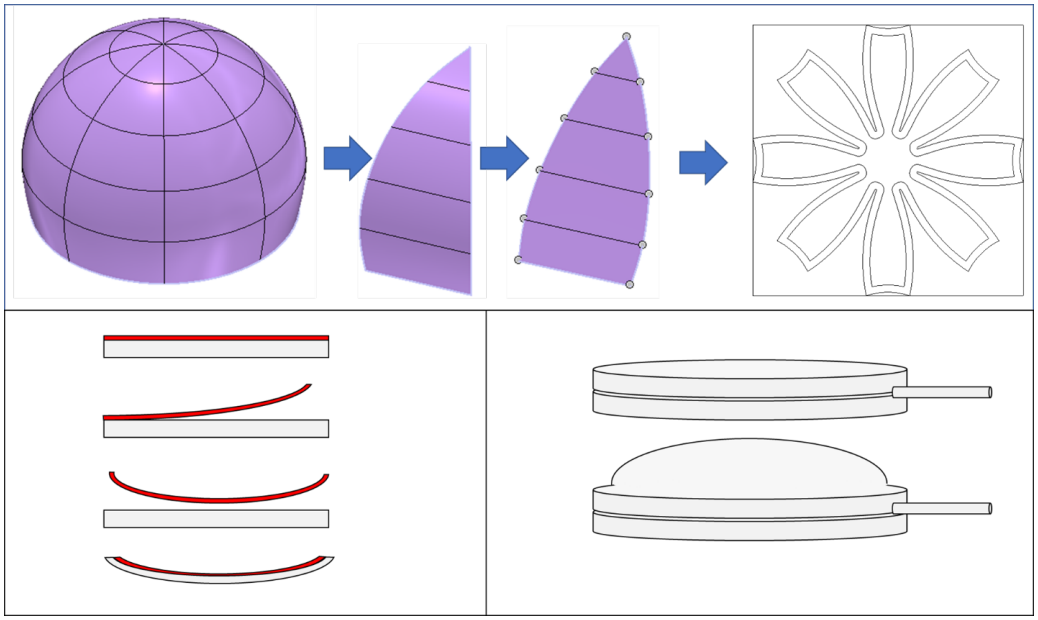

Figure 2.2: Design of lappets, application of prestrain, and swim bladder. Top: Lappets were designed in CAD by segmenting a hemisphere into eight lappets. The lappets were flattened into 2D and then arranged in an axisymmetric array to generate the design for the jellyfish-inspired robot. Bottom left: the acrylic elastomer (grey) comes affixed to a polyethylene liner (red). When the liner is removed, it exhibits some curvature. When we reapply the liner to the elastomer, the elastomer is prestrained slightly by the liner and demonstrates a similar curvature. Bottom right: The swim bladder is made from two layers of an acrylic elastomer that are adhered to each other around the border. A silicone tube is inserted between the layers and pressure is applied through the tube to inflate it, providing positive buoyancy for the jellyfish-inspired robot.

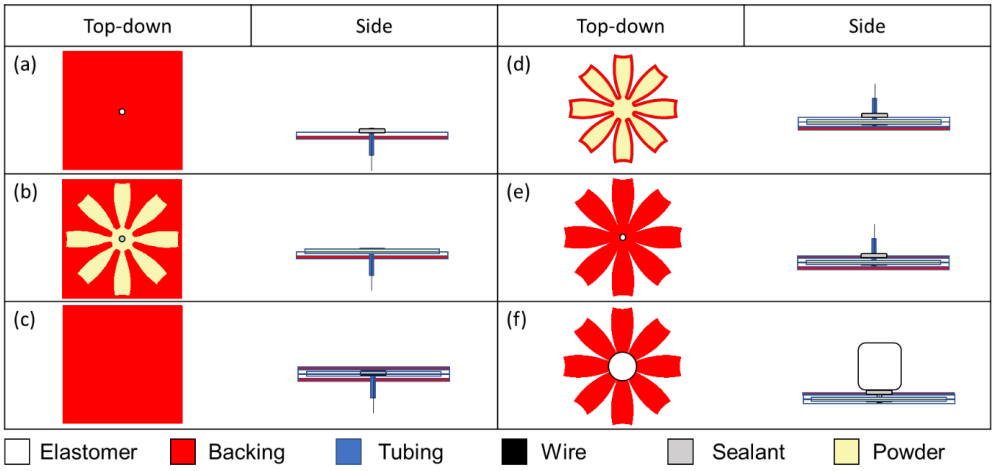

Figure 2.3: Fabrication process for FEDORA jellyfish. a) We prepare the back layer of the elastomer by cutting it to size and creating a hole in the center of the sheet where we insert a silicone tube and seal the tube to the elastomer with a silicone glue. For the untethered case, we thread a thin, flexible wire through the tubing to reduce the risk of an air in the tube causing an open circuit. b) We use a mask to apply a passivating powder to the lower elastomer layer and then (c) encase the powder with the dielectric elastomer layer. d) We remove the backing layer, seal the underside of the tube with silicone glue, and trim the excess material from the actuator through all layers using a laser cutter. After the sealing agent has cured, we inject the fluid electrode through the tubing using a syringe. (e) We reapply the backing layer to the under (tubing) side of the actuator. f) We connect the inner fluid electrode to the driving electronics, remove the backing layer from the dielectric elastomer layer, and apply a passivating agent to the outside of the dielectric elastomer to prevent unintended self-adhesion. For the tethered case, we electrically connect the high voltage power supply to the inner fluid electrode via a metallic syringe tip. For the untethered case, we seal the tubing shut using a nylon cable tie and electrically connect the power supply to the exposed wire. We then affix and seal the electronics to the robot using a silicone glue.

To generate the axisymmetric design for the jellyfish, we designed a hemisphere in CAD with eight segments or lappets (Figure 2.2). To enable fabrication of a 3D body using laminate fabrication techniques, we then flattened the hemisphere onto a planar projection and used layer-by-layer manufacturing to the assemble the structure, as shown in Figure

2.3. Fabrication details are provided in materials and methods.

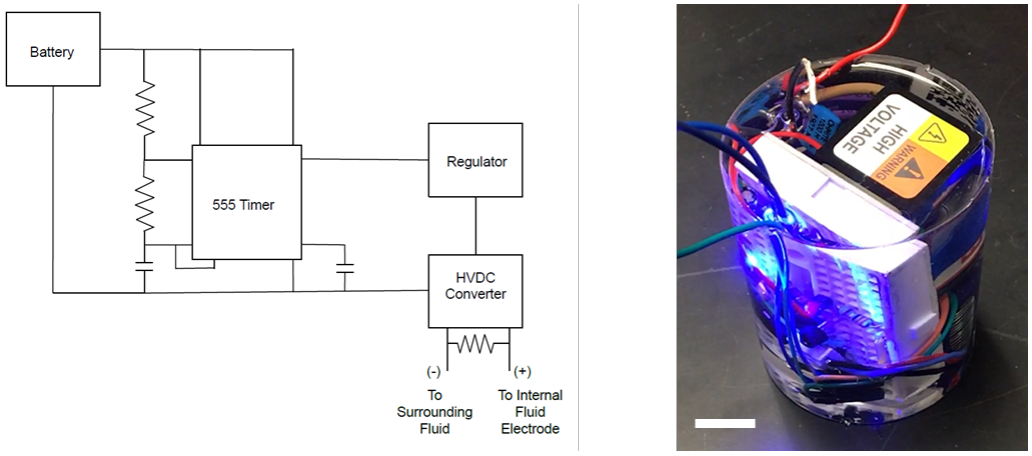

Figure 2.4: Untethered power supply. Left: schematic. A battery powers a 555 timer which we designed to provide a square wave output signal at a desired frequency and duty cycle. We connected the output of the timer to a voltage regulator that provides a consistent maximum voltage to the dc/high voltage dc (HVDC) convertor. The high voltage output of the HVDC convertor is connected to the inner fluid electrode and the ground output is connected to the surrounding fluid. Right: photo of power supply encased in silicone with its LED illuminated. Scale bar is 1 cm.

Design of untethered system

The untethered system needs to provide a high voltage signal to the inner fluid electrode with respect to the surrounding grounded fluid. To accomplish this, we attached a battery to a timing circuit that generates a low voltage square wave signal, as shown in Figure 2.4. The output of the timer powers a voltage regulator, which then triggers an LED and the high voltage DC/DC convertor. We connected the high voltage output of the HVDC convertor by wire to the internal fluid electrode and immersed the low voltage lead in the surrounding fluid to serve as a ground electrode. In these experiments we used tap water for the fluid electrodes, which we previously found to be sufficiently conductive

for actuation [75]. We placed a discharge resistor with a high impedance across the high voltage and ground leads to enable passive recovery of the actuators.

To provide buoyancy control, we assembled a swim bladder out of two layers of an acrylic elastomer using a similar fabrication approach as what was used for the actuators (see materials and methods). A tube was inserted in between the elastomer layers and we injected air with a syringe through a small tube to pressurize the swim bladder. The swim bladder was affixed to the upper surface of the jellyfish to provide buoyancy control. This configuration also has the benefit of reducing the risk of pull-in instability due to local deformation of the high voltage wire underneath.

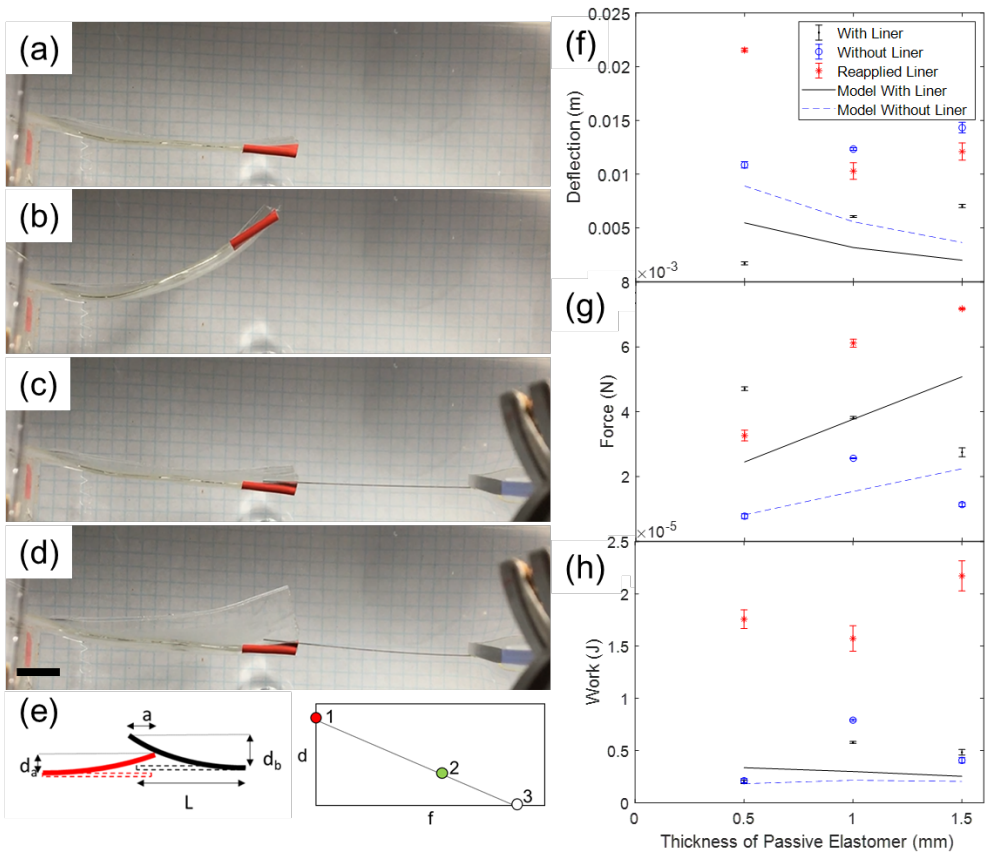

Figure 2.5: Static tests of unimorph FEDORAs to determine deflection, force, and work as a function of the thickness of the passive layer. Left column: deflection without force is taken as the difference of the position of the tip when the voltage is off (a) and on (b). Red tape is applied to the tip as a visual marker to help with tracking. To measure blocked force, we place a spring steel beam with length L next to the tip of the actuator (c) and measure the deflection of the beam (d_b) and actuator (d_a) when the voltage is on (d) as shown in the schematic (e). The beam overlaps the tip of the actuator a distance a. We use Euler-Bernoulli beam theory to calculate the force that the actuator imparted on the beam. To estimate the blocked force, we plot the displacement at no force (point 1) and the calculated force at a small displacement (d_a, point 2) and assume a linear relation between the force and displacement and extrapolate to determine the blocked force (point 3). Right column: comparison of analytical model and experimental results for (f) deflection, (g) blocked force, and (h) work as a function of the thickness of the elastomeric passive layer. Error bars are the standard deviation from three actuations for each actuator configuration. Scale bar is 1 cm.

Experimental Design

Measure deflection and force as a function of frequency for different actuator configurations

To determine optimal configurations for the actuators, we measured their maximum deflection and blocked force, as shown in Fig. 2.5. Using the same lateral geometry for each actuator (50.8 mm in width, 76.2 mm in length, with a passive border of 8 mm), we tested actuators with a passive layer thickness of 0.5 mm, 1 mm, and 1.5 mm. We tested the impact of an inextensible strain-limiting layer (the polyethylene backing that the acrylic elastomer is initially affixed to) on actuation. Each test begins with the liner applied (as supplied by the manufacturer), then we measure the actuator again after removing the liner. The acrylic elastomer was rolled up in a tube. When we remove the liner from the elastomer, the liner exhibits a curvature in the opposite direction as the curvature it had when it was on the tube. When we re-apply the liner to the elastomer, the elastomer is prestrained and curls slightly due to the curvature of the liner (Fig. 2.2). We suspended the actuators in water and applied a constant, fixed voltage (7 kV) and measured the maximum deflection. To determine the maximum blocked force, we placed a strip of spring steel with known dimensions adjacent to the actuator and measured the deflection of both the spring steel and actuator when we applied a voltage. Using Euler-Bernoulli beam theory, we calculated the corresponding force at this actuator displacement. Assuming a linear relationship between force and displacement, we extrapolated to find the blocked force. The area under the curve is calculated as the work output of the actuator. We then compared the work output for three thicknesses of passive layer (0.5, 1, and 1.5 mm) and three conditions of the inextensible backing (backing on, backing removed, and backing

reapplied).

Measure speed for tethered design To determine the maximum speed as a function of frequency, we attached the robot to a high voltage power supply and drove it at a fixed frequency. The robot was suspended by its silicone tubing which was affixed to a float to maintain a constant vertical position. A wire connected the fluid electrode to the high voltage electronics. Overhead video provided a record of the lateral position of the robot with respect to time and the videos were analyzed using Tracker [91].

Estimated power consumption and cost of transport

To estimate the mechanical power required to deform the actuator, we followed an approach described previously [75] which calculates the electrical input power to be $P_{electrical} = C_{act}V^2f$, based on the capacitance when the actuator is actuated (C_{act}), the applied voltage (V), and driving frequency (f). To find C_{act}, we measured the capacitance of the actuator in the rest state directly using an LCR meter and calculated the expected value of C_{act} based on the change in area and thickness that is predicted from Pelrine's equation and Hooke's law [2]. We then calculate the cost of transport as $COT = P/vmg$, where P is the electrical input power, v is the average velocity, m is the mass, and g is the gravitational constant [92].

Measure speed for untethered robot

To determine the ability of the robot to swim untethered, we sealed the wireless power supply to the robot and attached a pneumatic swim bladder to the top of it. We tuned the bladder so that the overall structure was slightly negatively buoyant, placed the robot at the bottom of a tank of water, and actuated it at a fixed frequency. We used video to record the position of the robot with respect to time as the robot swam to the top of the

tank of water.

RESULTS

Deflection, blocked force, and work of unimorph actuators

As the thickness of the passive layer increased from 0.5 mm to 1.5 mm, the deflection also increased (Fig. 2.5). For each thickness of passive layer, the deflection increased when the liner was removed. When the liner was reapplied, the deflection decreased, except in the case when the passive layer was the same thickness as the active layer. The model predicted that the deflection would be greater for the actuator without a liner versus with a liner, and that the deflection would decrease as the thickness of the passive layer increased. The greatest deflection that we measured was 2.2 cm for the actuator with 0.5 mm thick active and passive elastomer layers and the reapplied liner.

When the actuators were tested with the liner still affixed, the blocked force decreased as the thickness of the passive layer increased. The model predicted that the actuators with the liner would have a greater blocked force than the actuators without a liner and that the blocked force was proportional to the thickness of the passive layer and the trend of the actuators with the reapplied liner agreed with the prediction of the model. The maximum blocked force that we calculated was 7.2 mN for the 0.5/1.5 mm layers and the reapplied liner.

For actuators without an inextensible layer, the model predicted that a peak value of work exists when the passive layer is twice that of the active layer. In contrast, when there was an inextensible layer, the work decreased as the thickness of the passive layer increased. The experimental results for the two cases of the as-prepared liner and actuator without liner agreed with the trend predicted by the model for the case without a liner.

However, the actuators with reapplied liners showed the opposite trend. We calculated the maximum work to be 22 μW for the 0.5/1.5 mm layers and reapplied liner.

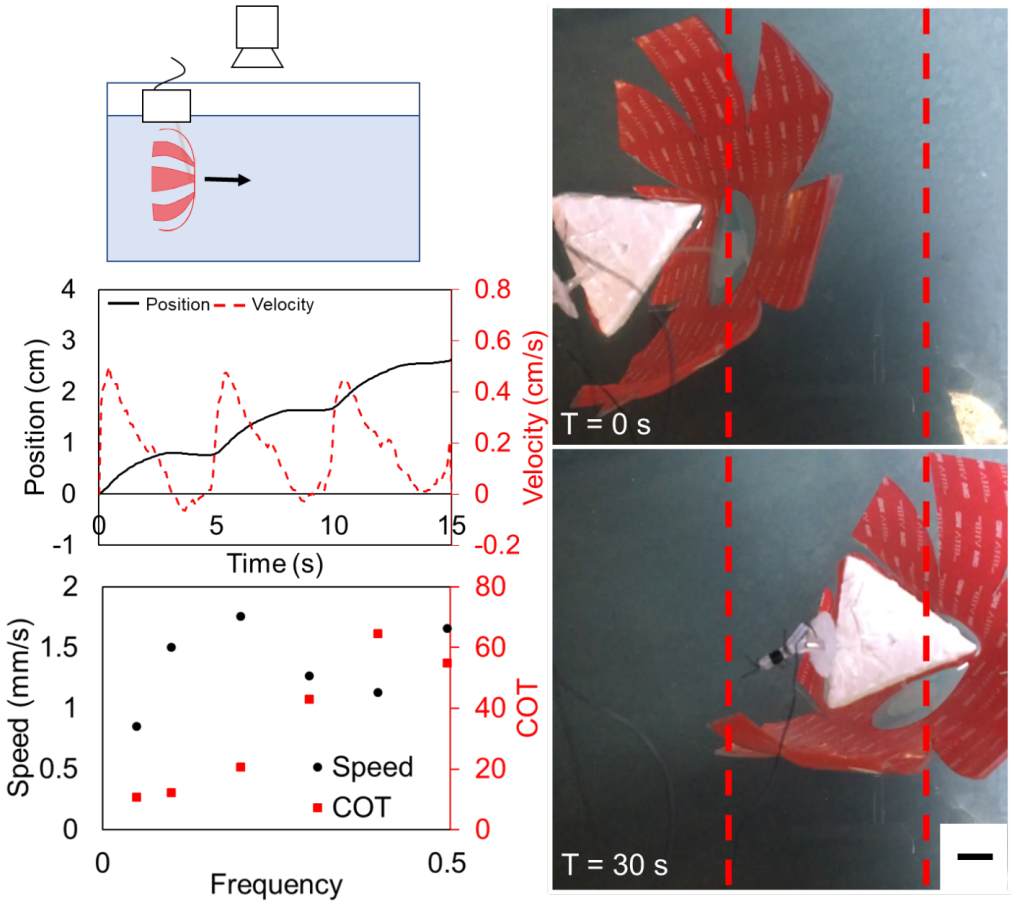

Figure 2.6: Tethered FEDORA jellyfish swimming results. Top left: schematic of experimental setup. Right: still frames taken from swimming tests at the beginning of the test (top) and after 30 seconds (bottom). Middle left: representative example of position and velocity as a function of time for three actuation cycles. Bottom left: Speed and cost of transport as functions of frequency, demonstrating a maximum speed of 1.8 mm/s and a corresponding COT of 21. Scale bar is 1 cm.

Tethered swimming performance

The motion of the robot is approximately sinusoidal with propulsion and coast

phases, which is qualitatively similar to jellyfish. The maximum average speed of the tethered robot was 1.8 mm/s at a driving frequency of 0.2 Hz, as shown in Fig. 2.6, with an instantaneous peak speed of 5 mm/s during contraction. The electrical input power P at 0.2 Hz was 20 mW and corresponding COT was 21.

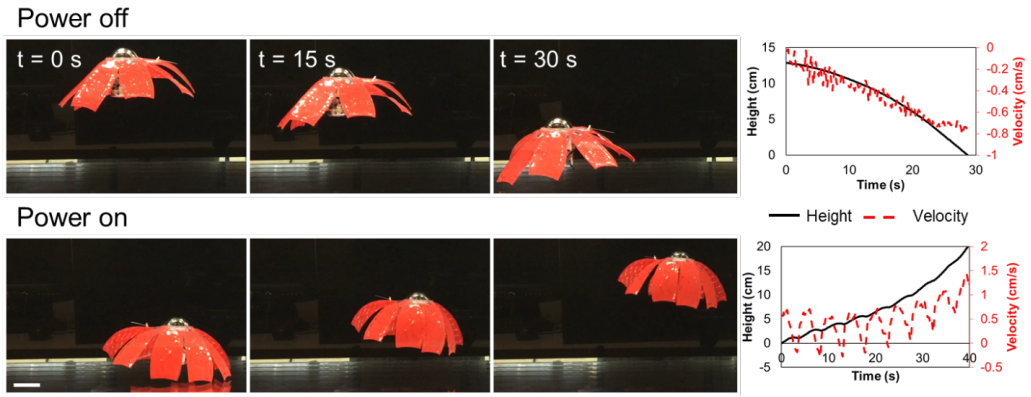

Figure 2.7: FEDORA jellyfish free-swimming results. Top row is when the robot is off demonstrating negative buoyancy. Bottom row is when the robot is swimming upward with a driving frequency of 0.2 Hz. Figures in the right column show the height from the bottom of the tank and velocity in the vertical direction as a function of time for both the falling (top) and swimming (bottom) cases. Scale bar is 5 cm.

Untethered swimming performance

The untethered jellyfish-inspired robot was driven at 0.2 Hz and the average speed over the first three cycles was 3.2 mm/s, as shown in Fig. 2.7, and the peak instantaneous speed was 7.1 mm/s. For a bell margin diameter of 16.3 cm, this corresponds to an average swimming speed of 0.02 BL/s. After three cycles, the upward velocity increased which was likely coupled with a positive change in buoyancy as the pressure on the swim bladder decreased. The COT for the untethered jellyfish was 2.8, due to the increase in velocity and mass of the robot compared to the tethered case. For this test, we used a battery with a

capacity of 180 mAh. The HVDC convertor consumed an average of 0.25 W to power the FEDORAs. At an average power input of 0.25 W and an average speed of 3.2 mm/s, we estimate that a 180 mAh battery would provide enough power for 2.7 hours of actuation.

DISCUSSION

As discussed in section 3.2, the model predicts maximum deflection for a unimorph actuator that behaves as a simple bilayer—i.e. for the case where both layers have the same thickness and modulus. However, when we use FEDORAs without a liner, both dielectric elastomer layers (top and bottom) should experience some strain, proportional to their thickness. In the case where the passive layer is thicker than the active layer, then the strain in the active layer should dominate. Interestingly, we still observed deflection for the case when both layers had the same thickness. This result may be due to our fabrication approach in which a passivating powder is applied to the passive layer which imparts some additional stiffness in the thickness direction of the passive layer, imparting the asymmetry necessary for bending.

As the model is unable to account for prestrain, we were unable to use it to predict the performance of the actuator when we reapplied the liner. The model successfully predicted that the deflection would be greater for an actuator without an inextensible layer and that the force would be greater with the inextensible layer. We also observed the trend that the work of the actuator without a liner would be the greatest when the thickness of the passive layer was twice that of the active layer. However, the trends of how the force and deflection scale with the thickness of the passive layer disagreed with our experimental results. This may be due to the model not taking Maxwell stress on the passive elastomer into account or that there is additional prestrain in the device due to the manufacturing

process.

We used the unimorph results to guide our design of the jellyfish-inspired robot. We selected the combination of layer thicknesses that would result in maximizing work for a fully elastomeric robot (0.5 mm thick DEA and 1 mm thick passive layer). To further increase the work, we also used the reapplied liner. Our experimental unimorph results suggest that we may be able to further increase the actuation of our jellyfish-inspired robot by using a thicker passive elastomer layer, but a full comparison between the performance of robots with different thicknesses of the passive layer is reserved for future work.

One challenge with this approach is that prestrain-free DEAs are incapable of providing large forces and thus high-speed propulsion. The maximum tethered and untethered speeds that we measured were 1.8 and 3.2 mm/s, respectively, which may be insufficient for applications in high flow, high speed environments. The speed of our untethered jellyfish is $\sim$3x slower than that of jellyfish of similar mass and the COT of our untethered jellyfish was $\sim$5x greater than that of a a jellyfish with a similar mass [78]. The development and employment of sensors, programmability, and lateral control is reserved for future work.

In this work, we developed a completely soft jellyfish-inspired robot in which all the components—aside from the driving electronics—were flexible or stretchable. The high voltage electrode is encapsulated within a dielectric membrane, ensuring that it is safe for use around animals. As with our previous work using fluid electrodes [75], the FEDORAs actuate completely silently as opposed to traditional ROVs that rely on propeller or jet propulsion, enabling stealthy locomotion. We demonstrate that a flexible but inextensible layer can apply a non-negligible prestrain for DEAs, creasing the performance of the

actuators. Many DEAs employ prestrain to improve their performance, but this approach typically requires a rigid frame to maintain that prestrain during actuation. By using an inextensible layer with an initial curvature, we were able to more than double the work output of our actuators without employing a rigid frame. Additionally, we developed a waterproof power supply and demonstrated untethered swimming of our jellyfish-inspired robot. The onboard power supply obviates the need for a tether or external magnetic or electric field. This proof-of-concept prototype demonstrates the feasibility of using FE-DORAs for driving bioinspired swimming robots for underwater applications where low power and silent locomotion are important.

MATERIALS AND METHODS

We used VHB 4905 (3M) for the 0.5 mm thick dielectric elastomers, VHB 4910 for the 1 mm thick elastomers, and a laminate of the two for 1.5 mm thick layers. Caster sugar was used as the passivating powder and dish soap was used as a passivating liquid. An EMCO Q101 high voltage power convertor was used as a voltage amplifier in all experiments.

ACKNOWLEDGEMENTS

This work was funded by the Office of Naval Research (ONR) grants N000141712062 and N00014-18-1-2277. C. Christianson was supported by National Science Foundation Graduate Research Fellowship grant number DGE-1144086.

Chapter 2, in full, has been submitted for publication of the material. Christianson, Caleb; Bayag, Christopher; Li, Guorui; Jadhav, Saurabh; Giri, Ayush; Agba, Chibuike; Li, Tiefeng; Tolley, Michael T. The dissertation author was the primary investigator and author of this paper.

Chapter 3

Cephalopod-Inspired Robot Capable of Cyclic Jet Propulsion Through Shape Change

Caleb Christianson,[1] Yi Cui,[2] Xiaobo Bi,[3] Qiang Zhu,[3] Geno Pawlak,[2] and Michael T. Tolley,[2*]

[1]Department of NanoEngineering, University of California San Diego, 9500 Gilman Dr., La Jolla, CA 92093.

[2]Department of Mechanical and Aerospace Engineering, University of California San Diego, 9500 Gilman Dr., La Jolla, CA 92093.

[3]Department of Structural Engineering, University of California San Diego, 9500 Gilman Dr., La Jolla, CA 92093.

Abstract

The compliance and conformability of soft robots provide inherent advantages when working around delicate objects or in unstructured terrain. However, rapid locomotion in soft robotics is challenging due to the slow propagation of motion in compliant structures, particularly in underwater environments. Cephalopods overcome this challenge using jet propulsion and the added mass effect to achieve rapid, efficient propulsion underwater without a skeleton. Taking inspiration from cephalopods, here we present an underwater robot with a compliant body that can achieve repeatable jet propulsion by changing its internal volume and cross-sectional area to take advantage of jet propulsion as well as the added mass effects. The untethered, free-swimming robot achieves a maximum average thrust of 0.19 N and maximum average and peak swimming speeds of 18.4 cm/s (0.54 body lengths/s) and 32.1 cm/s (0.94 BL/s), respectively. We also demonstrate the use of an onboard camera as a sensor for ocean discovery and environmental monitoring applications.

INTRODUCTION

It is challenging to realize fast motion in robots comprised of compliant materials. While rigid materials can have a rapid dynamic response, soft structures have a delay in propagation of motion that limits the rate of actuation. Previous research on making soft robots move quickly employed combustion [58,93,94], high pressure fluids [48], or energy storage in elastic materials coupled with a quick release [25, 95]. However, applications relying on combustion require fuel, which can be messy and impose safety concerns, and both combustion and pressurized fluids draw from a finite reservoir which can be rapidly depleted.

Previous research on agile swimming robots have employed both traditional pro-

pellers and novel biomimetic methods such as fish-like locomotion or jet propulsion. To date, most of the interest in biomimetic robots has been focused on fish-inspired systems with undulatory body motions and fin flapping [96–99]. These systems, however, are usually not able to reach the same level of performance (e.g. speed, maneuverability and efficiency) of their natural counterparts. This is mostly attributed to the complexity of fish swimming mechanism (e.g. the multi-degree-of-freedom control of the fins) that is difficult to duplicate in artificial systems. Cephalopods (e.g. squids), on the other hand, have demonstrated impressive instantaneous speeds during escape maneuvers through a much simpler propulsion mechanism in the jetting mode [100–102]. In this swimming method, the thrust force comes not only from the repulsive effect of the jet flow, but also from variations of the added mass when the cross-sectional area of the body changes during deformation [101, 103]. In such a case, a body capable of volume change can be much more efficient than a jet-propelled body with a rigid shell [17]. Research has shown that the squid can reach the fastest speeds among aquatic invertebrates [104]. In fact, its limit is comparable, if not higher than fish [105]. Previous research on jet propulsion in cephalopod-inspired robots with deformable bodies was either pre-strained and released by hand [19] or employed tendon-driven contraction of a soft shell [20]. The ultra-fast escape maneuver demonstrated by hyperinflation of the body achieved high acceleration with a collapsible body, but the motion was not cyclic as it had to be manually pressurized for each trial [19]. In the tendon-driven approach, the body was deformed in discrete places with relatively small volume change [20].

In this work, we developed a method for realizing repeatable jet propulsion in a squid-inspired robot that takes advantage of the added mass effect. We measured the

thrust and structure of the vortex rings for a range of driving frequencies and formation numbers. To enable free swimming, we developed and implemented a waterproof power supply, resulting in a top speed of 18.4 cm/s, corresponding to 0.54 body lengths/s (BL/s), and maximum instantaneous speed of 32.1 cm/s (0.94 BL/s). Additionally, we tested nozzles with different orientations with respect to the long axis of the robot to demonstrate turning maneuvers through thrust vectoring. This locomotion strategy may enable effective propulsion without a propeller, reducing the risk of the propulsion system of the robot to get ensnared or to cause damage to objects in its environment. Further, the high top speed enable evasive maneuvers such as rapid turns [48].

The rest of the paper is organized as follows: we begin by providing a brief review of cephalopod-inspired jet propulsion and the hypothesis for this work. Next, we lay out the design of the components of our experimental robotic platform and follow it up with a description and discussion of our experimental results. Finally, we provide an overall discussion of the findings and offer our conclusions and direction for future work.

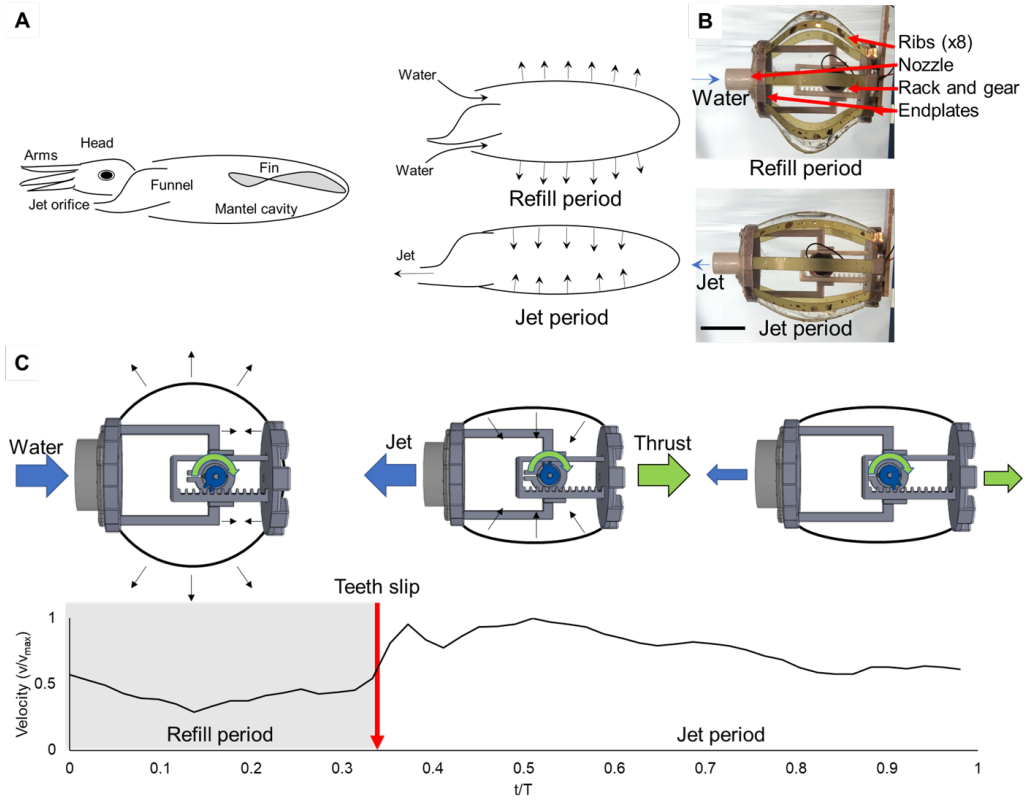

Figure 3.1: Principle of operation for cephalopod-inspired robot. **A** Mechanism for jet propulsion in squid. During the refill period, the mantle expands, drawing in water. When jetting, the mantle cavity contracts, expelling water through the nozzle. **B** Images of cephalopod-inspired robot in the refill period (top) and jet period (bottom). **C** Schematic of the slip-gear mechanism from the beginning of the refill period through the jet period of the cycle with a representative plot of the untethered swimming velocity over time for one cycle. The peak velocity was 29.4 cm/s and the frequency was 1.18 Hz. Scale bar is 5 cm.

RESULTS

Brief review of cephalopod-style jet propulsion and hypothesis for robotic system

Three concepts related to cephalopod-style jet propulsion that we aim to explore in this work are pulsed jets, the added mass effect, and an optimal nozzle based on the

volume of jetted fluid. To achieve jet propulsion, cephalopods cyclically hyperinflate their mantle with seawater and then rapidly expel it through a nozzle (Fig. 3.1) to generate pulsed jets of water, [15, 106]. Pulsed jets can be 50% more efficient than a steady jet due to the additional entrainment of the surrounding fluid and higher pressures at the leading edge of the vortex ring [16, 107, 108]. Another key component of cephalopod-inspired jet propulsion is the added mass effect [17, 18], in which a deformable body achieves an additional acceleration by reducing its overall volume (and thus its effective mass) during swimming. Lastly, to maximize propulsive efficiency, the jetted fluid needs to be entirely rolled up into a vortex ring, which occurs at an optimal ratio of the length of the jet to the diameter of the vortex ring (L/D), which is also referred to as the *formation number* [21]. Research has shown that the optimal ratio is 4 for starting jets and efficiency decreases for formation numbers that deviate away from it [109, 110].

In this work, we aim to develop a robot that is capable of cyclic, pulsed jet propulsion through changes in its overall volume to take advantage of the added mass effect. We hypothesize that we can achieve maximum efficiency and thrust for a configuration of the robot that results in a formation number with a value of approximately four.

Design of compliant structure to allow for a change in volume during actuation

The design of our robot was based on a compliant structure that can change both its overall volume and cross-sectional area during swimming (Fig. 3.1B). To achieve volume change, the body of the robot comprises an axisymmetric array of high aspect ratio, flexible beams affixed at either end by two rigid endplates (Fig. 3.1C). The high aspect ratio shape of the beam enabled axial compression allowing the body to shrink length-wise while providing torsional stiffness to avoid relative rotation at the rigid endplates along the long-

axis. As the internal volume increased, so did the cross-sectional area of the robot. In the fully inflated state, the beams and skin stored elastic energy that drove the deflation during the jet period (Figs. 3.1, 3.6). The material and thickness of the compliant beams were chosen to be flexible enough to enable buckling during the refill period while storing enough elastic energy to drive the jet period, ([111], and similar to an approach that has been used to achieve efficient legged locomotion [112]). The two rigid endplates held the ends of the beams in place and provided hubs to mount the motor, transmission mechanism, nozzle, and electronics. The endplates were designed to be sufficiently rigid to avoid deformation during the actuation cycle. The ribs were inserted into slots in the endplates which were angled slightly away from the long axis of the robot to ensure the bending of the beams outwards during axial compression (Fig. 3.1B). To encapsulate the internal volume of fluid, we fit an elastomeric skin to the body on the outside of the compliant ribs. The elastomeric skin deformed with the body throughout the actuation cycles and stores 37% additional elastic energy (0.273 J of the 1.000 J total stored in the body of the robot) during the refill period which is released during the jet period of the cycle (Fig. 3.6).

Transmission mechanism for power amplification

To enable gradual storage of fluid and elastic energy and fast release, we designed a slip-gear transmission mechanism (Fig. 3.1C). The gear was mounted to a motor which was affixed to the rear plate of the robot and the rack was attached to the front plate. Driven by the motor, the gear traveled up the rack, pulling the two end plates closer to each other and causing the beams to buckle outwards. When the gear reached the point that the teeth were no longer engaged with the rack, the elastic restoring force of the compliant beams

and elastomeric skin triggered the jet period of the robot, during which the internal volume and cross-sectional area were decreased, and a jet flow is formed behind. This inflation-deflation cycle was repeated so that the system swam via intermittent bursts.

Nozzle design

An important parameter in jet propulsion is the formation number, a dimensionless parameter that is associated with vortex structure in the jet that is determined by the volume change of the robot and the diameter of the nozzle [18, 21, 110, 113]. For our robot, the formation number can be calculated as $F = 4(V_f - V_i)/\pi D^3$, where V_f and V_i are the final and initial volumes of the body and D is the inner diameter of the nozzle [18]. Specifically, it has been demonstrated that for a squid starting from rest, a formation number of four leads to optimal peak speed after the ejection [18]. For a fixed change in volume of the robot, we can change the diameter of the nozzle to ensure that the robot is operating near this optimal formation number. (Alternatively, we could fix the nozzle diameter and vary the change in volume of the robot, but this option is practically more difficult.)

We attached a nozzle to the end of the robot to direct the flow of fluid in and out of the internal chamber. The simplest configuration uses the same nozzle as the flow inlet. This design deviates from the actual morphology of squids, which have separate inlets and outlets. We also examined the option of using one-way valves to allow additional inflow. To do this, we introduced holes around the base of the nozzle and attached a passive flap that serves as a one-way valve (Fig. 3.7). The flap deflected passively to allow additional fluid to enter during the refill period and closed during the jet period, forcing all the fluid to exit through the outlet nozzle. We hypothesized that this squid-inspired configuration would increase the thrust of the robot.

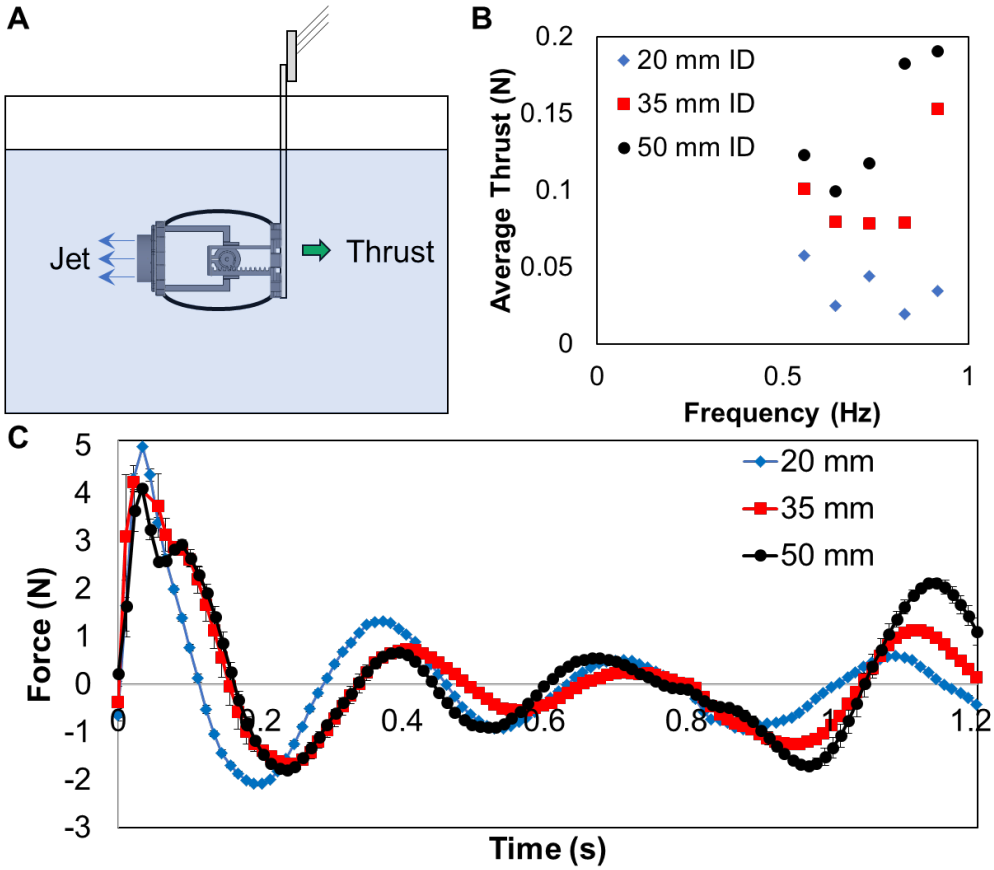

Figure 3.2: Schematic of experimental setup and results for thrust measurements. **A** We attached the robot to a beam that is affixed to a rigidly mounted load cell. **B** Plot of average thrust over five cycles as a function of frequency for three different nozzle diameters. **C** Force as a function of time for each of the three nozzle diameters. The plot begins just before the jet period of the cycle. The primary peak is due to the reaction force as the robot ejects a plume of fluid. The sinusoidal signal is caused by oscillations of the robot and the beam that the robot was attached to for testing. The minima between t = 0.8 s and t = 1 s is caused by the refill period of the cycle. The error bars are the standard deviation for three cycles.

Investigation of thrust as a function of frequency for different formation numbers

To measure the thrust generated by the robot, we affixed it to the end of a beam

and submerged it underwater (Fig. 3.2). We bolted the beam to a load cell that was rigidly mounted to a frame above the water tank. To characterize the dependence of the thrust on formation number and actuation frequency, we affixed nozzles with three different inner diameters (IDs) to the tethered robot and actuated it at five frequencies between 0.56 and 0.92 Hz while measuring the average thrust. The IDs of the nozzles were 20 mm, 35 mm, and 50 mm, corresponding to formation numbers of 56, 10, and 3.6. As shown in Fig. 3.2B, the average thrust is the lowest across all frequencies for the largest formation number tested and was the greatest for the nozzle corresponding to a formation number $\sim$4. The average thrust also increased as the frequency increased. We measured a maximum thrust (0.190 N) for a nozzle diameter of 50 mm at 0.92 Hz, which corresponded to a formation number of $\sim$4. We plot the thrust as a function of time for a fixed frequency (0.83 Hz) for each of the nozzle IDs, each averaged over three trials (Fig. 3.2C). The plot begins immediately prior to the slip condition of the robot, right before the ejection of the jet. As the gear slipped, the elastic restoring force of the beams and elastomeric skin drove the endplates of the robot apart, ejecting a jet of fluid, thus imparting a thrust force upon the load cell. The oscillations shown in the figure are due to the dynamics of the robot and the beam that we mounted the load cell to. The decrease in thrust between t = 0.8 s and t = 1.0 s corresponds to the subsequent compression cycle as the robot began to suck in more fluid resulting in a negative thrust. While the highest average instantaneous thrust is shown for the nozzle with the smallest ID, the duration of the thrust was shorter than that for the larger nozzles. Instead, we can compare the impulse (area under the force-time curve) for the three nozzle IDs. The impulses were 65.8 mN-s, 171 mN-s, and 186 mN-s for the 20, 35, and 50 mm nozzle IDs, respectively.

We also measured the thrust as a function of frequency for the nozzle with a passive, one-way valve and compared it to the thrust of the nozzle with the same diameter (Fig. 3.7). While the maximum thrust at the highest frequency was higher for the nozzle without the valve, the thrust of the nozzle with the valve was more consistent across the tested frequencies and was greater than the thrust of the valveless nozzle at lower frequencies.

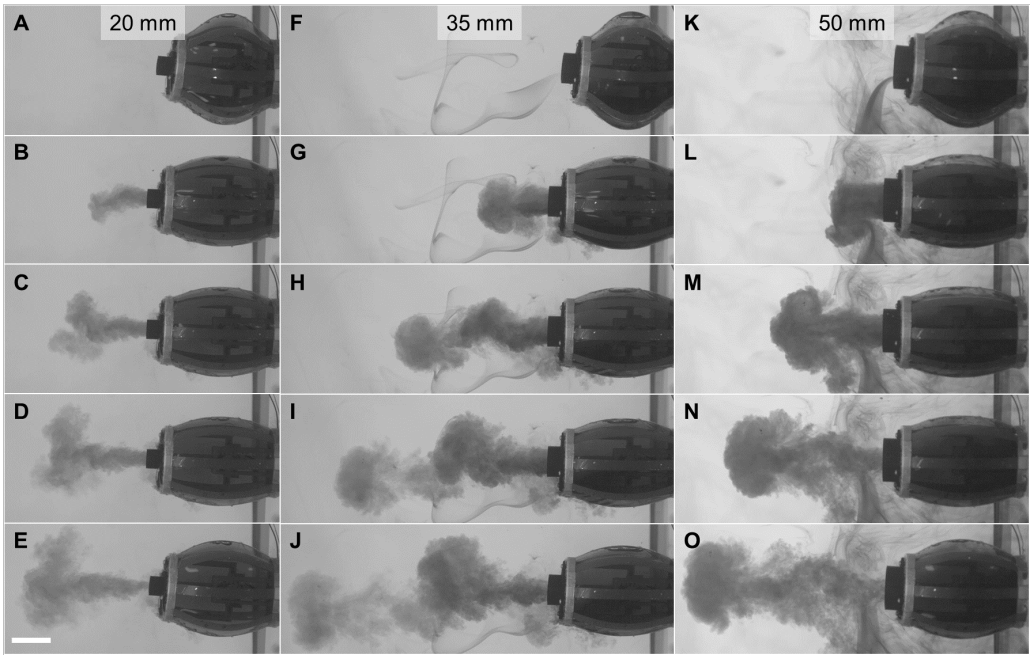

Figure 3.3: Visualization for structure of the ejected flow. Still-frame captures from a flow visualization experiment, where we loaded the robot with dye and captured the jet structure at 1000 fps for nozzle diameters of 20 mm (left), 35 mm (center), and 50 mm (right). Images are 0.24 seconds apart and the scale bar is 5 cm.

Characterization of the structure of the vortex rings

We assessed the characteristics of the outflow jet using flow visualization experiments. To do this, we mounted the robot to a rigid plate with dye injected into the internal

volume prior to initiation of the motion cycle. High speed video of jets expelled through nozzles of three diameters allowed us to resolve the evolution of vortical structure in the jet (Fig. 3.3).

The formation number is a measure of the jet duration relative to the optimal time for vortex ring formation [21]. Maximum thrust per pulse is achieved at a formation number of 4. The ejected jet should be entirely wrapped up in the primary vortex ring to maximize the vortex size [21]. For the 20 mm diameter nozzle, corresponding to a formation number of 56, a vortex ring formed early in the cycle (Fig. 3.3C), but broke down rapidly and was overtaken by the continuing jet flow (Fig. 3.3E). For the 35 mm diameter case (formation number = 10), a more stable leading vortex ring was apparent (Fig. 3.3G), but jet flow continued with some of the subsequent jet fluid degenerating into a secondary vortex (Fig. 3.3I), reducing the overall efficiency. For the 50 mm diameter nozzle (formation number = 3.6), a single large vortex ring was generated (Fig. 3.3M-O), indicating optimal efficiency for jet propulsion.

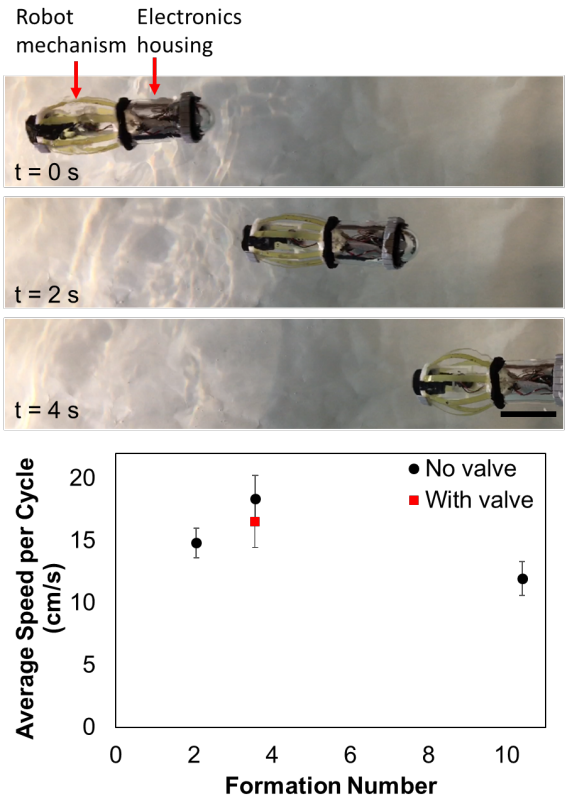

Figure 3.4: Untethered swimming. Top: screen captures from swimming with the battery powered electronics. Bottom: Average speed per cycle as a function of different formation numbers based on nozzle diameter, including the 50 mm ID nozzle with a passive one-way valve. Error bars are the standard deviation for five cycles and the scale bar is 10 cm.

Untethered swimming

To demonstrate free swimming, we developed a waterproof container to house the power supply and electronics for driving the robot (Fig. 3.9). We designed the container to be large enough to house a camera and additional sensors, if desired. We then measured the average speed per actuation cycle for three nozzle diameters, corresponding to formation numbers of 2.1, 3.6, and 10. As shown in Fig. 3.4, the highest average swimming speed (18.4 ± 1.8 cm/s, corresponding to 0.54 BL/s) was found for the nozzle with a formation

number closest to 4 at an actuation frequency of 1.12 Hz, based on a battery voltage of 12 V. The refill period lasted for 35% of the total cycle. We also measured the average swimming speed for the nozzle with a set of passive, one-way valves and a formation number of 3.6 and found its speed to be 16.5 $\pm$ 2 cm/s. While the valves increased the average thrust of the robot at some frequencies (see Fig. 3.7), this decrease in the overall speed of the untethered robot implies that the valves reduced the effectiveness of the jet propulsion in this optimal case, most likely due to increased fluid drag.

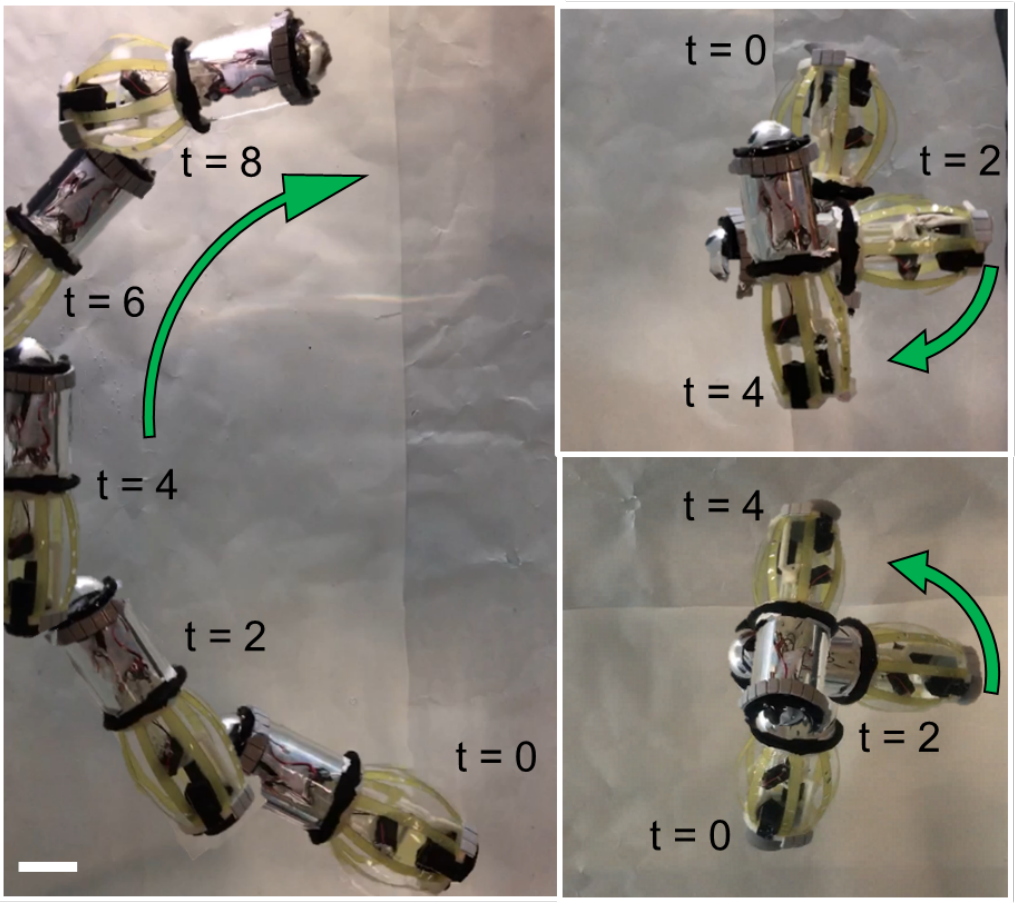

Figure 3.5: Control of turning radius and direction with thrust vectoring. Left is a compilation of overlaid still frames from controlled clockwise swimming with a 17° angle nozzle. Right is counterclockwise (top) and clockwise (bottom) swimming with a -34° and 34° angle nozzle, respectively. Time between frames is two seconds and the scale bar is 5 cm.

Thrust vectoring

To demonstrate the capability of the robot to turn based on thrust-vectoring of the nozzle, we 3D-printed nozzles with fixed angles relative to the long-axis of the robot of 17°, 34°, and -34°, and measured the turning radius for each during swimming (Fig. 3.5). The radii of curvature for the 17°, 34°, and -34° nozzles were 36.8 cm, 6.3 cm, and 7.6 cm,

respectively. The turning rates were 20 °/s, 44 °/s, and 50 °/s. The difference between the speed and radii for the 34° and -34° nozzles is due to a slight offset between the orientation of the nozzle and the plane of turning, which caused some rotation out of the plane.

Power consumption

We connected the motor of the robot to a benchtop power supply and recorded the power required to drive the motor as a function of the voltage applied to the motor as a function of actuation frequency (Fig. 3.8). The power consumed increased linearly with the actuation frequency (R^2 = 0.9672). We calculated a maximum electrical input power of 6.9 W per cycle when the robot was actuating at 0.92 Hz, which was the maximum actuation frequency for the thrust measurements. At 6.9 W per cycle, an 11.1 volt, 1000 mAh battery could operate for over an hour-and-a-half of continuous swimming. Using the linear relationship between frequency and power consumption described above, we compared the power input to the estimated power output based on the average thrust from our thrust measurements and the average swimming speed from our untethered swimming experiments. To measure the efficiency of the robot, we compared the estimated mechanical output power to the electrical input power ($\varepsilon = P_{mech}/P_{elec} = Fv/P_{elec}$). For an actuation frequency of 0.92 Hz, thrust of 190 mN, and swimming speed of 18.4 cm/s, the robot had an efficiency of 0.51%. While control of the driving frequency of the robot is beyond the scope of this work, we estimated the efficiency at the lowest frequency for which we measured the thrust (0.56 Hz) using the same value for speed (18.4 cm/s) and calculate a power efficiency of 0.54%. This demonstrates that we may be able to tune the driving frequency to optimize for low power consumption or high speed. The maximum power output of the motor was 1.7 W at an efficiency of 20% [114]. Assuming that we were

driving the motor near its limit, the mechanical power efficiency ($\varepsilon = P_{mech\_out}/P_{mech\_in}$) of the robot was 2.1%. These results suggest that we can further improve the overall efficiency of the robot by selecting a more efficient motor and driving it closer to its optimal performance range by optimizing the design of the transmission mechanism.

Storage of elastic energy in the robot

While the skin was crucial to providing an enclosed volume for the robot to constrain the internal fluid, it also played a role in elastic energy storage during actuation. To measure the contribution of the elastic energy in the ribs and skin, we placed the robot in a uniaxial compression test fixture and measured the stress-strain curve (Fig. 3.6) both with the elastomeric skin on and with it off. The curves had a bilinear shape; both structures were rigid at the start and then become more compliant as the beams buckled outward. The skin added a longer high-stiffness region, resulting in more energy storage during the refill period of the cycle, as seen in the increased area under the force-displacement curve. Of the 1.0 Joules of work done to compress the body by 3 cm, 27% of it was due do the contribution of the skin.

Lifetime of the robot

For this early, proof-of-concept prototype, the robot was generally able to operate on the order of $\sim$5000 cycles before failure. Failure was primarily caused by degradation of the 3D printed gear. The D-shaped shaft of the motor would deform the D-shaped slot in the gear, preventing it from rotating with the shaft. This could be corrected in a future version by manufacturing the gear out of a more rigid material. Another source of intermittent failure was caused when the motor mount would lose tension on the motor, causing it to spin freely. This could be addressed by improving the robustness of the motor

mount in future designs. The final source of failure observed was in degradation of the flexible beams, in which they would fracture at their bases from cyclic stresses imparted by the end-plates. An improvement to the design of the sockets where the beams were held in place may further improve the longevity of the robot.

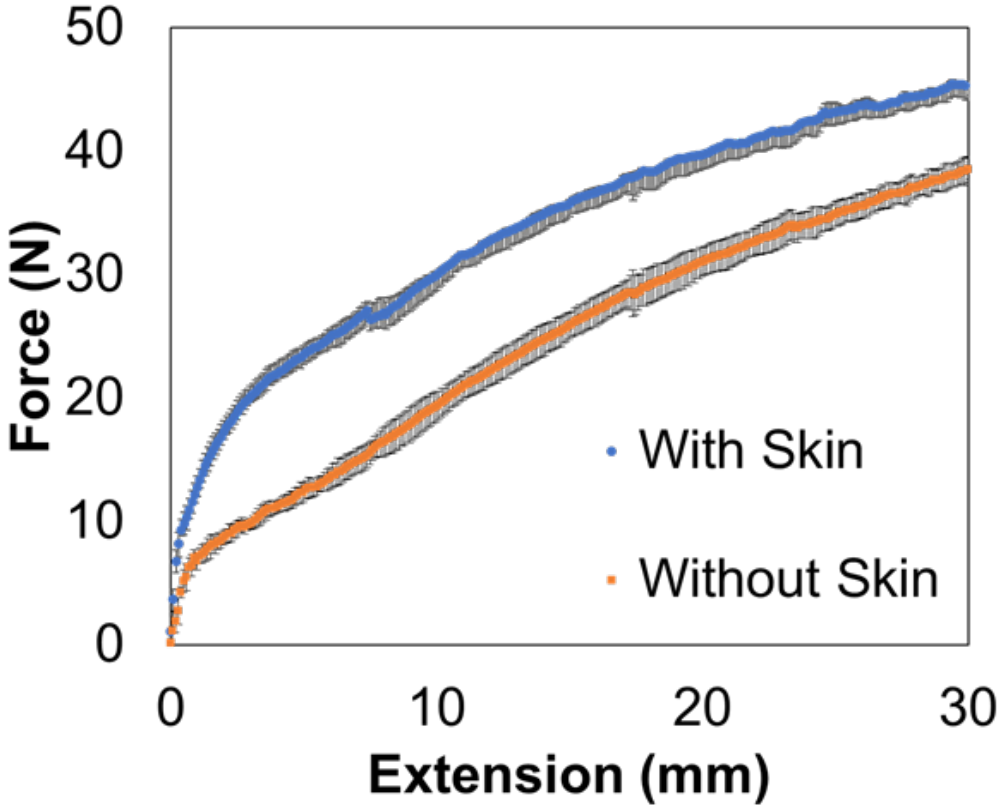

Figure 3.6: Measurement of energy storage in the body of the robot.Using a uniaxial compression test fixture, we measured the force as a function of compression of the robot both with the elastomeric skin on and with it off.

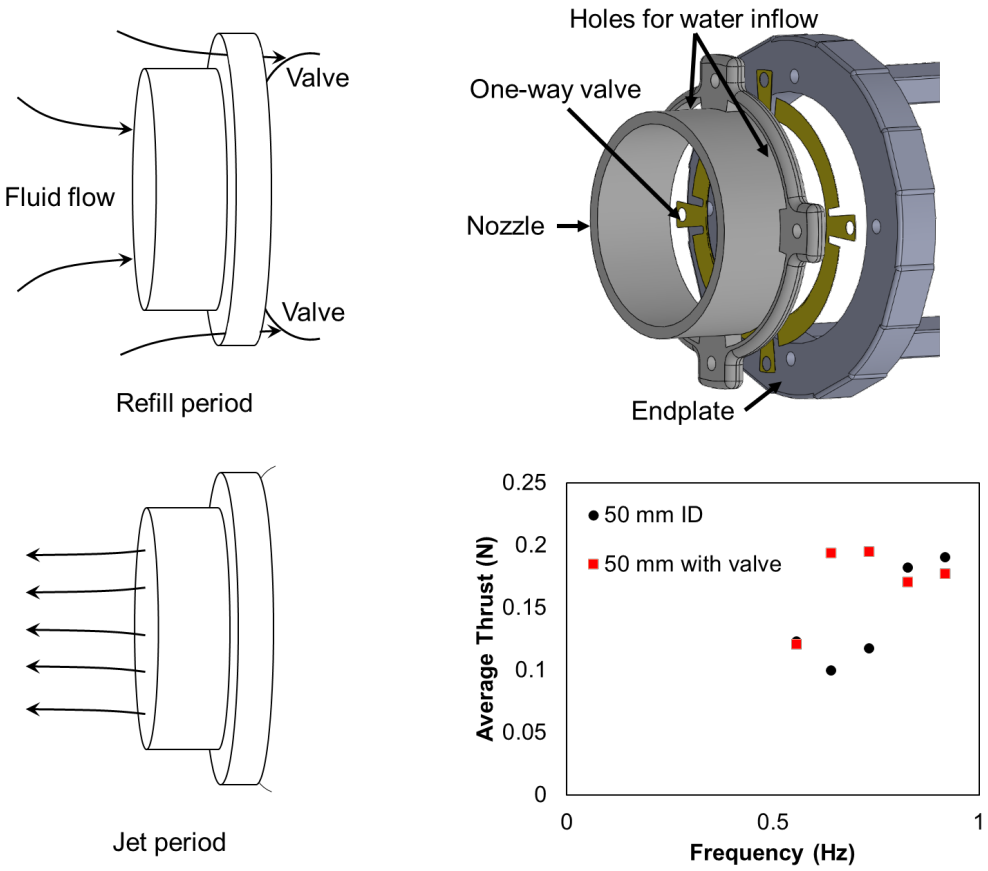

Figure 3.7: Nozzle with passive valve. During the refill period (top left), the passive valves open, allowing water to flow in around the perimeter of the nozzle as well as through the center of the nozzle. During the jet period (bottom left), the one-way valves shut, forcing the fluid out through nozzle. Top right: CAD of nozzle with passive, one-way valve with key features labeled. Bottom right: thrust as a function of frequency for the 50 mm ID nozzle with the holes and one-way valve (flap) and without. The performance is similar for both, although we do see a more consistent thrust profile for lower frequencies with the one-way valve. In free swimming tests, the robot was actuated in the higher frequency range presented here, and the speed for the nozzle with the valve was less than that of the robot with the regular nozzle, consistent with these results. These results indicate that for free swimming at lower frequencies, the valve may improve performance.

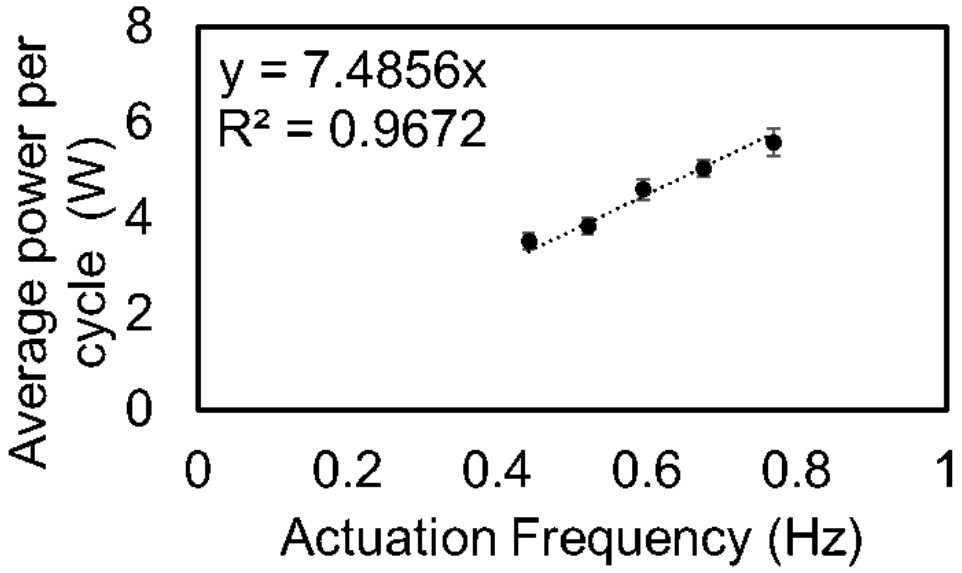

Figure 3.8: Power consumption as a function of frequency. To determine the amount of power required to drive the robot, we used a benchtop power supply to power the robot at input voltages from 8 to 12 V and recorded the power consumption as a function of voltage. Each voltage corresponds to an actuation frequency of the robot, and we've plotted the average power consumption per cycle as a function of actuation frequency.

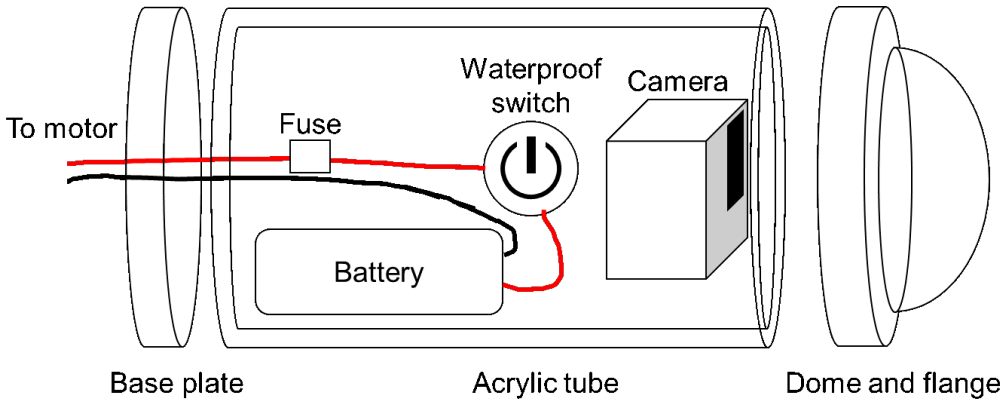

Figure 3.9: Waterproof housing for electronics. In an early prototype of a waterproof housing for the electronics, we sealed an acrylic tube to an acrylic base plate and inserted a flange that held an acrylic dome in place. Within the housing, we connected the wires from the motor to a battery and a waterproof switch. We also included a fuse for safety. We designed the housing to be sufficiently large to include room for a camera as well as other sensing payloads if desired in future work.

DISCUSSION

In this work, we demonstrated a free swimming, cephalopod-inspired robot capable of cyclic jet propulsion through shape change with a top average speed of 18.4 cm/s. This design approach enabled repeatable slow storage and rapid release of elastic energy to generate pulsed jets while taking advantage of the added mass effect. We optimized our robot design based on the formation number, adjusting the diameter of the outlet nozzle to maximize the energy transferred to the surrounding fluid. However, the relationship between formation number and optimal thrust is a function of ambient motion [113], so the ideal volume ejected per pulse will change as the speed of the robot changes. The optimal formation number is also sensitive to the acceleration profile for the jet [115], so the volume rate of change for the robot may also play a role in optimizing thrust. We measured a maximum thrust of 0.190 N, which is comparable to what has been

reported for squid [116]. Our results indicate that this type of robot could be operated in either high speed or low power consumption modes based on the driving voltage. We also demonstrated controlled turning of the robot using thrust vectoring. The high speed, pulsatile locomotion makes the robot effective for agile escape maneuvers such as rapid turns [106]. Additionally, the robot demonstrated high reliability ($\sim$5000 cycles between repairs) and was fabricated from 3D printed and commercial-off-the-shelf (COTS) components. While the center portion of the body is compliant, one challenge with the existing design compared to biological squid is that the endplates are rigid, constraining the diameter of openings that the robot could swim through. One opportunity for improvement is in the motor and transmission mechanism—motors are not as good in cyclic loading and our design places a heavy, cyclic load on the motor during the refill period. An improved design may be able to more efficiently store elastic energy while minimizing the cyclic load to the motor. Additionally, as with all other robots that use elastic materials under cyclic deformation, material selection is important to ensure sufficient lifetime for the robot.

To further improve the performance of the robot, one could optimize the design of the nozzle to increase the thrust generated per cycle [117]. Additionally, it may be possible to improve the passive one-way valve design to increase the efficiency of the robot. In future work, it could be possible to implement controllable nozzles to enable dynamic control of thrust vectoring and active steering. Additionally, more sophisticated electronics would enable speed control to tune for either low power consumption or high speed. Additionally, the inclusion of a sensor suite to monitor analytes of interest in the ocean (e.g., pH, temperature, salinity, etc.) is reserved for future work. Further, the ability to 3D print the entire body (including the flexible ribs) may further facilitate rapid manufacturing of

future prototypes. The performance of the robot could be further increased with a slip gear that has many more teeth to allow a smaller motor to achieve the same compression when turned on only during the compression period and off during the coast period (instead of running continuously, requiring such a large gap between the teeth). The optimization of the gear and timing of the robot to reduce the impact of power consumption on the motor and battery is reserved for future work.

The proof-of-concept platform described in this paper has the potential to enable applications in underwater exploration and sampling where moderate velocities (e.g., in non-negligible currents) are important. The cyclic intake of water into the internal volume of the robot may allow for dynamic, discrete water sampling during swimming. Additionally, as the robot uses cyclic, pulsed jet propulsion that takes advantage of the added mass effect, it may be used as a platform for studying and better understanding cephalopod locomotion.

MATERIALS AND METHODS

Robot fabrication

We designed the body of the robot (end plates, motor mount, gear, and rack) in CAD and printed the body out of polylactic acid (PLA) using a Prusa i3 MK3 3D printer (Prusa Research, Czech Republic). We laser-cut the compliant beams from a sheet of 0.015" thick Garolite G-10/FR4. We used VHB 4905 from 3M for the elastomeric skin. We used a 195:1, 12 V brushed DC gearmotor from Pololu, item number #3481, to drive the gear.

Force measurements

To measure the force, we connected the motor of the robot to a microcontroller with

a motor driver (Arduino). We connected the robot to a straight bar load cell (TAL220B, SparkFun Electronics) and used a microcontroller (Arduino) to record the signal, which was amplified with an HX711 load cell amplifier (SparkFun Electronics).

Flow visualization

To visualize the jet vortices, we used Sheaffer blue ink to dye the water. We recorded the vortices at 1000 frames per second using a Photometrics high speed camera.

Untethered swimming

For the untethered robot, we used a 20 C, 11.1 V, 1000 mAh lithium ion polymer battery from to Floureon provide power. We built the waterproof housing from a 3" diameter acrylic tube, domed end cap, and flange (Blue Robotics Inc.) and sealed the housing with marine epoxy (Loctite).

ACKNOWLEDGEMENTS Funding: This work was funded by Office of Naval Research (ONR) grants N000141712062 and N000141812277. CC was supported by National Science Foundation Graduate Research Fellowship grant number DGE-1144086. **Author contributions:** CC, QZ, and MT conceived of the project. CC and YC designed, fabricated, and tested the robot. CC, QZ, GP, and MT analyzed the data. QZ, GP, and MT provided guidance for the project. All authors contributed to the final version of the manuscript. **Competing interests:** The authors declare no competing interests. **Data and materials availability:** Data is available from the authors upon request.

Chapter 3, in full, has been submitted for publication of the material. Christianson, Caleb; Cui, Yi; Bi, Xiaobo; Zhu, Qiang; Pawlak, Geno; Tolley, Michael T. The dissertation author was the primary investigator and author of this paper.

Chapter 4

Conclusion

In this work I explored actuation for bioinspired, soft, swimming robots. I primarily explored three major research questions: 1) How can I achieve swimming with frameless, bidirectional DEAs underwater? In pursuit of this, I also discovered that my approach enabled silent, transparent, elastomeric actuators for eel-like swimming. 2) How can I optimize the layers of a laminate DEA for bending to create the active stroke and passive recovery of jellyfish-inspired propulsion? 3) How can I optimize the design and actuation of a deformable, cephalopod-inspired robot to take advantage of both pulsatile jet propulsion and the added mass effect?

To explore the first question of how to achieve swimming with frameless, bidirectional DEAs underwater, I developed a bimorph actuator comprised of DEAs with fluid for electrodes (FEDEA). I measured the bending as a function of actuator length and applied voltage and compared it to an analytical model with good agreement. To test the ability of the FEDEA bimorph to swim, I imparted asymmetry in the structure via an in-

extensible plastic strip on the front and enabled the actuator to propel itself against the surface tension of the water that it was submerged in to generate forward propulsion. To demonstrate the efficacy of fluid as electrodes, I measured the amplitude of actuation over time for four cases: an actuator with carbon grease electrodes in air (1) and water (2), and actuators with fluid electrodes submerged in water with either USP-grade pure water (3) or 35 g/L saltwater (4) as the inner electrode. The results with the saltwater fluid electrode demonstrate the maximum performance in terms of actuation amplitude. However, the small decrease in performance between a starting stream of salty water (4) and pure water (3) demonstrate that any purity of water is sufficient for actuation at high voltages, likely due to the contamination of ions during the fabrication process or that are absorbed from the environment over time.

To test the acoustic stealth of the actuators, we measured the sound level as a function of frequency across the audible spectrum (20 Hz to 20 kHz) and observed that the active and rest state of the actuators resulted in no significant change in the measured sound level. However, the actuators were driven at a lower frequency (0.3 Hz) than the instruments that I used were able to detect. A measurement of infrasound around the actuation frequency may be able to detect some noise which could be noticeable to marine species, but was not completed during this study.

I tested the passive camouflage of the robot by measuring the transmittance of visible light through two regions of the robot (the active area, where the electrodes are, and the passive border, where the two layers of elastomer adhere to each other) and compared it to the transmittance of a leptocephalus across the visible spectrum. I observed that the transmittance of the outside border and active area served as lower and upper bounds,

respectively, for the transmittance of the eel across the visible spectrum, demonstrating that, on average, the eel-inspired robot is as translucent as a leptocephalus. To demonstrate the ability of the robot to fluoresce to enable visual communication, I loaded the fluid electrode with a fluorescent dye and stimulated it with ultraviolet light. The transparency of the elastomer and fluid electrodes enable the transmission of fluorescent light and the signal was detectable after 48 hours.

To enable anguilliform-inspired locomotion, I affixed three bimorph FEDEAs end-to-end and actuated them with a controlled sequence to generate an undulating, propulsive wave through the body of the robot. To reduce the impact of the tension from the tethers on the locomotion of the robot, I suspended the robot from a swinging arm, which held the robot as a fixed distance and allowed it to swim along an arc. The results of this project were the first published work demonstrating that water could be used as both electrodes in a DEA for a robot, the first paper to quantify the transparency and acoustic profile of a DEA with fluid electrodes, and I demonstrated that DEAs without prestrain can be used for underwater locomotion.

To answer the second question of how to optimize the layers of a laminate DEA for bending to create the active stroke and passive recovery of jellyfish-inspired propulsion, I explored two main hypotheses: 1) unimorph actuators based on DEAs with an appropriate selection of properties (e.g., thickness and Young's modulus) for each of the layers can enable pulsatile motion, sufficient for underwater locomotion and 2) a straightforward control strategy, sufficient for achieving the pulsatile motion of a jellyfish, enables untethered propulsion. I began by designing a unimorph actuator with an active DEA layer, a passive elastomeric layer, and a strain-limiting layer comprised of a polyethylene liner. When I

applied a voltage to the inner fluid electrode with respect to the surrounding fluid, Maxwell forces compressed the active layer, causing it to bend toward the side of the strain-limiting layer. To design the geometry of the actuator so that it could be fabricated in flat layers and then bent into an approximation of a 3D hemisphere, I designed a hemisphere in CAD, sectioned it into eights, flattened a single lappet, and then rotated the design into an axisymmetric array of eight lappets. While still only an approximation of a fully curved hemisphere, this design approach enabled laminate manufacturing of 2D layers into a 3D shape.

To validate the concept via tethered locomotion, I suspended the robot by its tube to a floating platform and actuated it through a range of frequencies to find the driving frequency that would result in a maximum speed and efficiency. In our work, the frequency that maximized speed was 0.2 Hz. For the range of frequencies tested, the efficiency (defined as the cost of transport, COT), decreased as the driving frequency decreased. I would expect that there should be some frequency that would result in a minimum of the COT, but it was not uncovered in the range of frequencies that we tested.

To produce an untethered robot, I designed and fabricated a waterproof, high voltage power supply consisting of a 555 timer, which generates a square wave with a controllable frequency and duty cycle, a voltage regulator, a high voltage convertor, and a discharge resistor. I encased the electronics in silicone to waterproof them. I then connected the high voltage power supply to the fluid electrodes to generate motion. For the free-swimming test, I affixed a buoyancy device to the top surface of the robot and tuned the robot to be slightly negatively buoyant. I then turned the voltage on and demonstrated free, upwards swimming of the robot with an average speed of 3.2 mm/s. This resulted in

the first untethered, jellyfish-inspired robot based on prestrain-free DEAs and the fastest untethered, jellyfish-inspired robot based on DEAs.

To answer the third question of how to optimize the design and actuation of a deformable, cephalopod-inspired robot to take advantage of both pulsatile jet propulsion and the added mass effect, I tested five main hypotheses: a slip-gear mechanism can enable slow storage and rapid release of elastic energy; beams and an elastomeric skin can store sufficient elastic energy to drive pulsed jet propulsion; the thrust of the robot can be optimized for the right ratio of jet length to diameter; valving to provide unidirectional flow will improve the performance of the robot; and angled nozzles may enable turning based on thrust vectoring.

I demonstrated that a simple design of a slip gear could effectively slowly store and quickly release the elastic energy stored up in the beams and elastomeric skin. I measured the thrust as a function of nozzle diameter and frequency, and demonstrated that the nozzle diameter corresponding to a formation number of 4 generated the most thrust across all frequencies that we tested. I recorded the evolution of the vortex structure via high speed flow visualization and observed that the stability of the leading vortex was maximized for the nozzle diameter that corresponded to a formation number of four. I designed and implemented a simple, one-way valve to implement unidirectional flow in the robot and observed an increase in average thrust at low frequencies compared to the valve-less case, but similar performance at higher frequencies.

I designed a waterproof electronics housing to hold the battery, fuse, sensors, and other electronics and measured the untethered swimming speed as a function of formation number, marking a maximum in speed for a formation number of four.

Finally, I was able to demonstrate controlled turning through thrust vectoring by affixing nozzles with different angles with respect to the long axis of the body, and showed that we could control the radius and direction of turning based on the angle of the nozzle.

In this work, I demonstrated both pulsed jet propulsion and acceleration based on the added mass effect; the dependency of both thrust and swimming speed based on the formation number, controlled turning through thrust vectoring, and a straightforward, reliable electromechanical control system that enabled untethered propulsion.

These results demonstrate three approaches to actuate bioinspired, soft, swimming robots with different performance characteristics. Depending on the needs of the project, the appropriate actuation approach could be selected. For example, if the project required a robot that was transparent, silent, flexible, and consumed low power, and the speed of the robot wasn't a concern (e.g., for studying acoustic signals underwater or searching for elusive species), then the actuation approach in the eel-inspired robot may be a good fit. On the other hand, if noise and transparency weren't as important as speed and thrust (e.g., structural diagnostics or mapping coral reefs), then the actuation approach demonstrated in the cephalopod-inspired robot may be more appropriate. With this approach, the appropriate actuation strategy could be selected for the task at hand. These results demonstrate actuation strategies for realizing bioinspired locomotion in soft, swimming robots capable of going through tight spaces, safe interaction with the environment or humans, and could be useful for applications in structural diagnostics, environmental monitoring, or search and rescue.

Bibliography

[1] R. E. Pelrine, R. D. Kornbluh, and J. P. Joseph, "Electrostriction of polymer dielectrics with compliant electrodes as a means of actuation," *Sensors and Actuators, A: Physical*, vol. 64, no. 1, pp. 77–85, 1998.

[2] R. Pelrine, R. Kornbluh, Q. Pei, and J. Joseph, "High-speed electrically actuated elastomers with strain greater than 100%," *Science*, vol. 287, no. 5454, pp. 836–839, 2000.

[3] F. Carpi, I. Anderson, S. Bauer, G. Frediani, G. Gallone, M. Gei, C. Graaf, C. Jean-Mistral, W. Kaal, G. Kofod, M. Kollosche, R. D. Kornbluh, B. Lassen, M. Matysek, S. Michel, S. Nowak, B. OBrien, Q. Pei, R. Pelrine, B. Rechenbach, S. Rosset, H. R. Shea, B. O'Brien, Q. Pei, R. Pelrine, B. Rechenbach, S. Rosset, and H. R. Shea, "Standards for dielectric elastomer transducers," *Smart Materials and Structures*, vol. 24, no. 10, p. 25, 2015.

[4] C. Keplinger, J. Y. J.-Y. J.-Y. Sun, C. C. Foo, P. Rothemund, G. M. Whitesides, and Z. Suo, "Stretchable, transparent, ionic conductors," *Science*, vol. 341, no. 6149, pp. 984–987, 2013.

[5] P. Brochu and Q. Pei, "Advances in dielectric elastomers for actuators and artificial muscles," *Macromolecular Rapid Communications*, vol. 31, no. 1, pp. 10–36, 2010.

[6] L. An, F. Wang, S. Cheng, T. Lu, and T. J. Wang, "Experimental investigation of the electromechanical phase transition in a dielectric elastomer tube," *Smart Materials and Structures*, vol. 24, no. 3, p. 035006, 2015.

[7] S. Rosset and H. R. Shea, "Flexible and stretchable electrodes for dielectric elastomer actuators," *Applied Physics A: Materials Science and Processing*, vol. 110, no. 2, pp. 281–307, 2013.

[8] D. McCoul, W. Hu, M. Gao, V. Mehta, and Q. Pei, "Recent Advances in Stretchable and Transparent Electronic Materials," *Advanced Electronic Materials*, vol. 2, no. 5, pp. 1–51, 2016.

[9] F. Carpi, P. Chiarelli, A. Mazzoldi, and D. De Rossi, "Electromechanical characterisation of dielectric elastomer planar actuators: Comparative evaluation of different electrode materials and different counterloads," *Sensors and Actuators, A: Physical*, vol. 107, no. 1, pp. 85–95, 2003.

[10] B. Tavakol, M. Bozlar, C. Punckt, G. Froehlicher, H. A. Stone, I. A. Aksay, and D. P. Holmes, "Buckling of dielectric elastomeric plates for soft, electrically active microfluidic pumps," *Soft Matter*, vol. 10, no. 27, pp. 4789–4794, 2014.

[11] O. A. Araromi, S. Rosset, and H. R. Shea, "High-Resolution, Large-Area Fabrication of Compliant Electrodes via Laser Ablation for Robust, Stretchable Dielectric Elastomer Actuators and Sensors," *ACS Applied Materials and Interfaces*, vol. 7, no. 32, pp. 18046–18053, 2015.

[12] T. Li, G. Li, Y. Liang, T. Cheng, J. Dai, X. Yang, B. Liu, Z. Zeng, Z. Huang, Y. Luo, T. Xie, and W. Yang, "Fast-moving soft electronic fish," *Science Advances*, vol. 3, p. e1602045, 4 2017.

[13] J. Shintake, H. Shea, and D. Floreano, "Biomimetic underwater robots based on dielectric elastomer actuators," *IEEE/RSJ International Conference on Intelligent Robots and Systems*, vol. 2, pp. 4957–4962, 2016.

[14] J. Shintake, V. Cacucciolo, D. Floreano, and H. Shea, "Soft robotic grippers," *Advanced Materials*, vol. 1707035, no. May, 2018.

[15] A. Packard, "Jet propulsion and the giant fibre response of loligo," *Nature*, vol. 221, pp. 875–877, 3 1969.

[16] P. F. Linden, "The efficiency of pulsed-jet propulsion," *Journal of Fluid Mechanics*, vol. 668, pp. 1–4, 2011.

[17] G. D. Weymouth and M. S. Triantafyllou, "Ultra-fast escape of a deformable jet-propelled body," *Journal of Fluid Mechanics*, vol. 721, pp. 367–385, 2013.

[18] X. Bi and Q. Zhu, "Numerical investigation of cephalopod-inspired locomotion with intermittent bursts," *Bioinspiration and Biomimetics*, vol. 13, no. 5, 2018.

[19] G. D. Weymouth, V. Subramaniam, and M. S. Triantafyllou, "Ultra-fast escape maneuver of an octopus-inspired robot," *Bioinspiration and Biomimetics*, vol. 10, no. 1, p. 16016, 2015.

[20] F. Giorgio-Serchi, A. Arienti, and C. Laschi, "Underwater soft-bodied pulsed-jet thrusters: Actuator modeling and performance profiling," *International Journal of Robotics Research*, vol. 35, no. 11, pp. 1395–1416, 2016.

[21] M. Gharib, E. Rambod, and K. Shariff, "A universal time scale for vortex ring formation," *Journal of Fluid Mechanics*, vol. 360, pp. 121–140, 1998.

[22] R. D. Kornbluh, R. Pelrine, J. Joseph, R. Heydt, Q. Pei, and S. Chiba, "High-field electrostriction of elastomeric polymer dielectrics for actuation," *Proceedings of SPIE*, vol. 3669, no. 1, pp. 149–161, 1999.

[23] I. A. Anderson, T. A. Gisby, T. G. McKay, B. M. O'Brien, and E. P. Calius, "Multi-functional dielectric elastomer artificial muscles for soft and smart machines," *Journal of Applied Physics*, vol. 112, no. 4, pp. 0–20, 2012.

[24] F. Carpi, S. Bauer, and D. De Rossi, "Stretching dielectric elastomer performance," *Science*, vol. 330, no. 6012, pp. 1759–1761, 2010.

[25] D. Rus and M. T. Tolley, "Design, fabrication and control of soft robots," *Nature*, vol. 521, no. 7553, pp. 467–475, 2015.

[26] C. Murray, D. McCoul, E. Sollier, T. Ruggiero, X. Niu, Q. Pei, and D. D. Carlo, "Electro-adaptive microfluidics for active tuning of channel geometry using polymer actuators," *Microfluidics and Nanofluidics*, vol. 14, no. 1-2, pp. 345–358, 2013. EAP device that changes the shape of microfluidic channel.

[27] B. Tavakol and D. P. Holmes, "Voltage-induced buckling of dielectric films using fluid electrodes," *Applied Physics Letters*, vol. 108, no. 11, p. 112901, 2016.

[28] H. Godaba, J. Li, Y. Wang, and J. Zhu, "A soft jellyfish robot driven by a dielectric elastomer actuator," *IEEE Robotics and Automation Letters*, vol. 1, no. 2, pp. 624–631, 2016.

[29] S. Hsien Low, L. Lynn Shiau, and G. K. Lau, "Large actuation and high dielectric strength in metallized dielectric elastomer actuators," *Applied Physics Letters*, vol. 100, no. 18, 2012.

[30] B. Chen, J. J. Lu, C. H. Yang, J. H. Yang, J. Zhou, Y. M. Chen, and Z. Suo, "Highly stretchable and transparent ionogels as nonvolatile conductors for dielectric elastomer transducers," *ACS Applied Materials and Interfaces*, vol. 6, no. 10, pp. 7840–7845, 2014.

[31] X. Ji, S. Rosset, and H. R. Shea, "Soft tunable diffractive optics with multifunctional transparent electrodes enabling integrated actuation," *Applied Physics Letters*, vol. 109, no. 19, 2016.

[32] N. Bowden, S. Brittain, A. G. Evans, J. W. Hutchinson, and G. M. Whitesides, "Spontaneous formation of ordered structures in thin," *Nature*, vol. 393, no. May, pp. 146–149, 1998.

[33] D. H. Kim and J. A. Rogers, "Stretchable electronics: Materials strategies and devices," *Advanced Materials*, vol. 20, no. 24, pp. 4887–4892, 2008.

[34] D. H. Kim, J. Xiao, J. Song, Y. Huang, and J. A. Rogers, "Stretchable, curvilinear electronics based on inorganic materials," *Advanced Materials*, vol. 22, no. 19, pp. 2108–2124, 2010.

[35] R. Verplancke, F. Bossuyt, D. Cuypers, and J. Vanfleteren, "Thin-film stretchable electronics technology based on meandering interconnections: Fabrication and mechanical performance," *Journal of Micromechanics and Microengineering*, vol. 22, no. 1, p. 015002, 2012.

[36] J. N. Lee, C. Park, and G. M. Whitesides, "Solvent Compatibility of Poly(dimethylsiloxane)-Based Microfluidic Devices," *Analytical Chemistry*, vol. 75, no. 23, pp. 6544–6554, 2003.

[37] A. Poulin, L. Maffli, S. Rosset, and H. Shea, "Interfacing dielectric elastomer actuators with liquids," *Proceedings of Electroactive Polymer Actuators and Devices (EAPAD)*, vol. 943011, no. April, p. 943011, 2015.

[38] J. A. Rogers, "A clear advance in soft actuators," *Science*, vol. 341, no. 6149, pp. 968–969, 2013.

[39] P. Calvert, "Hydrogels for soft machines," *Advanced Materials*, vol. 21, no. 7, pp. 743–756, 2009.

[40] M. Bozlar, C. Punckt, S. Korkut, J. Zhu, C. Chiang Foo, Z. Suo, and I. A. Aksay, "Dielectric elastomer actuators with elastomeric electrodes," *Applied Physics Letters*, vol. 101, no. 9, 2012.

[41] H. Godaba, C. C. Foo, Z. Q. Zhang, B. C. Khoo, and J. Zhu, "Giant voltage-induced deformation of a dielectric elastomer under a constant pressure," *Applied Physics Letters*, vol. 105, no. 11, 2014.

[42] C. Christianson, N. Goldberg, S. Cai, and M. T. Tolley, "Fluid electrodes for submersible robotics based on dielectric elastomer actuators," p. 101631O, 2017.

[43] H. Yuk, S. Lin, C. Ma, M. Takaffoli, N. X. Fang, and X. Zhao, "Hydraulic hydrogel actuators and robots optically and sonically camouflaged in water," *Nature Communications*, vol. 8, pp. 1–12, 2017.

[44] K. Wang, G. Ouyang, X. Chen, and H. Jakobsen, "Engineering electroactive dielectric elastomers for miniature electromechanical transducers," *Polymer Reviews*, vol. 57, no. 3, pp. 369–396, 2017.

[45] P. Sommer-Larsen, G. Kofod, M. H. Shridhar, M. Benslimane, and P. Gravesen, "Performance of dielectric elastomer actuators and materials," *Society of Photo-Optical Instrumentation Engineers (SPIE) Conference Series*, vol. 4695, no. 1, pp. 158–166, 2002.

[46] S. Michel, X. Q. Zhang, M. Wissler, C. Löwe, and G. Kovacs, "A comparison between silicone and acrylic elastomers as dielectric materials in electroactive polymer actuators," *Polymer International*, vol. 59, no. 3, pp. 391–399, 2010.

[47] M. J. Lighthill, "Aquatic animal propulsion of high hydromechanical efficiency," *Journal of Fluid Mechanics*, vol. 44, no. 2, pp. 265–301, 1970.

[48] A. D. Marchese, C. D. Onal, and D. Rus, "Autonomous soft robotic fish capable of escape maneuvers using fluidic elastomer actuators," *Soft Robotics*, vol. 1, no. 1, pp. 75–87, 2014.

[49] M. J. Lighthill, "Note on the swimming of slender fish," *Journal of Fluid Mechanics*, vol. 9, no. 2, pp. 305–317, 1960.

[50] M. J. Lighthill, "Large-Amplitude Elongated-Body Theory of Fish Locomotion," *Proceedings of the Royal Society B: Biological Sciences*, vol. 179, no. 1055, pp. 125–138, 1971.

[51] E. D. Tytell, "The hydrodynamics of eel swimming: I. Wake structure," *Journal of Experimental Biology*, vol. 207, no. 11, pp. 1825–1841, 2004.

[52] G. S. Triantafyllou, M. S. Triantafyllou, and M. A. Grosenbaugh, "Optimal thrust development in oscillating foils with application to fish propulsion," 1993.

[53] J. R. Taylor, J. M. Gilleard, M. C. Allen, and D. D. Deheyn, "Effects of CO2-induced pH reduction on the exoskeleton structure and biophotonic properties of the shrimp Lysmata californica," *Scientific Reports*, vol. 5, no. April, pp. 1–12, 2015.

[54] A. Holzinger, M. C. Allen, and D. D. Deheyn, "Hyperspectral imaging of snow algae and green algae from aeroterrestrial habitats," *Journal of Photochemistry and Photobiology B: Biology*, vol. 162, pp. 412–420, 2016.

[55] D. F. Gruber, J. P. Gaffney, S. Mehr, R. Desalle, J. S. Sparks, J. Platisa, and V. A. Pieribone, "Adaptive evolution of Eel fluorescent proteins from fatty acid binding proteins produces bright fluorescence in the marine environment," *PLoS ONE*, vol. 10, no. 11, pp. 1–20, 2015.

[56] C. Mazel, "Method for Determining the Contribution of Fluorescence to an Optical Signature, with Implications for Postulating a Visual Function," *Frontiers in Marine Science*, vol. 4, no. August, pp. 1–12, 2017.

[57] N. Farr, A. Bowen, J. Ware, C. Pontbriand, and M. Tivey, "An integrated, underwater optical/acoustic communications system," *OCEANS'10 IEEE Sydney, OCEANSSYD 2010*, vol. 2, no. June 2010, 2010.

[58] N. W. Bartlett, M. T. Tolley, J. T. Overvelde, J. C. Weaver, B. Mosadegh, K. Bertoldi, G. M. Whitesides, and R. J. Wood, "A 3d-printed, functionally graded soft robot powered by combustion," *Science*, vol. 349, no. 6244, pp. 161–165, 2015.

[59] K. Kumar, J. Liu, C. Christianson, M. Ali, M. T. Tolley, J. Aizenberg, D. E. Ingber, J. C. Weaver, and K. Bertoldi, "A biologically inspired, functionally graded end effector for soft robotics applications," *Soft Robotics*, vol. 00, no. 00, p. soro.2017.0002, 2017.

[60] L. U. Odhner, L. P. Jentoft, M. R. Claffee, N. Corson, Y. Tenzer, R. R. Ma, M. Buehler, R. Kohout, R. D. Howe, and A. M. Dollar, "A compliant, underactuated hand for robust manipulation," *International Journal of Robotics Research*, vol. 33, no. 5, pp. 736–752, 2014.

[61] P. Polygerinos, N. Correll, S. A. Morin, B. Mosadegh, C. D. Onal, K. Petersen, M. Cianchetti, M. T. Tolley, and R. F. Shepherd, "Soft robotics: Review of fluid-driven intrinsically soft devices; manufacturing, sensing, control, and applications in

human-robot interaction," *Advanced Engineering Materials*, vol. 19, no. 12, pp. 1–22, 2017.

[62] C. Christianson, N. N. Goldberg, and M. T. Tolley, "Elastomeric diaphragm pump driven by fluid electrode dielectric elastomer actuators (fedeas)," *Electroactive Polymer Actuators and Devices (EAPAD) XX*, no. March, p. 21, 2018.

[63] F. A. Mohd Ghazali, C. K. Mah, A. AbuZaiter, P. S. Chee, and M. S. Mohamed Ali, "Soft dielectric elastomer actuator micropump," *Sensors and Actuators, A: Physical*, vol. 263, no. January, pp. 276–284, 2017.

[64] W. S. Chu, K. T. Lee, S. H. Song, M. W. Han, J. Y. Lee, H. S. Kim, M. S. Kim, Y. J. Park, K. J. Cho, and S. H. Ahn, "Review of biomimetic underwater robots using smart actuators," *International Journal of Precision Engineering and Manufacturing*, vol. 13, no. 7, pp. 1281–1292, 2012.

[65] Q. Shen, T. Wang, J. Liang, and L. Wen, "Hydrodynamic performance of a biomimetic robotic swimmer actuated by ionic polymer-metal composite," *Smart Materials and Structures*, vol. 22, no. 7, 2013.

[66] E. D. Tytell, "The hydrodynamics of eel swimming: I. wake structure," *Journal of Experimental Biology*, vol. 207, no. 11, pp. 1825–1841, 2004.

[67] "Trident underwater drone | openrov underwater drones," 0. [Online; accessed 2017-10-23].

[68] "Turnigy aerodrive dst-700 brushless outrunner motor 700kv," 0. [Online; accessed 2017-10-25].

[69] C. Larson, B. Peele, S. Li, S. Robinson, M. Totaro, L. Beccai, B. Mazzolai, and R. Shepherd, "Highly stretchable electroluminescent skin for optical signaling and tactile sensing," *Science*, vol. 351, no. 6277, pp. 1071–1074, 2016.

[70] M. J. Miller, R. Rutgers, B. Haythorne, T. Yavuzdoan, S. Obata, T. Wu, H. Rutgers, J. Powell, and K. Tsukamoto, "Observations of large muraenid leptocephali in coastal indonesia: Locations of sightings and behaviour of the larvae," *Marine Biodiversity Records*, vol. 6, no. Figure 1, p. e82, 2013.

[71] M. Dunbabin and L. Marques, "Robots for environmental monitoring: Significant advancements and applications," *IEEE Robotics and Automation Magazine*, vol. 19, no. 1, pp. 24–39, 2012.

[72] R. B. Wynn, V. A. Huvenne, T. P. Le Bas, B. J. Murton, D. P. Connelly, B. J. Bett, H. A. Ruhl, K. J. Morris, J. Peakall, D. R. Parsons, E. J. Sumner, S. E. Darby, R. M. Dorrell, and J. E. Hunt, "Autonomous underwater vehicles (auvs): Their past, present and future contributions to the advancement of marine geoscience," *Marine Geology*, vol. 352, pp. 451–468, 2014.

[73] J. S. Jaffe, P. J. Franks, P. L. Roberts, D. Mirza, C. Schurgers, R. Kastner, and A. Boch, "A swarm of autonomous miniature underwater robot drifters for exploring submesoscale ocean dynamics," *Nature Communications*, vol. 8, pp. 1–8, 2017.

[74] S. Bauer, S. Bauer-Gogonea, I. Graz, M. Kaltenbrunner, C. Keplinger, and R. Schwdiauer, "25th anniversary article: A soft future: From robots and sensor skin to energy harvesters," *Advanced Materials*, vol. 26, no. 1, pp. 149–162, 2014.

[75] C. Christianson, N. N. Goldberg, D. D. Deheyn, S. Cai, and M. T. Tolley, "Translucent soft robots driven by frameless fluid electrode dielectric elastomer actuators," *Science Robotics*, vol. 3, p. eaat1893, 4 2018.

[76] C. A. Aubin, S. Choudhury, R. Jerch, L. A. Archer, J. H. Pikul, and R. F. Shepherd, "Electrolytic vascular systems for energy-dense robots," *Nature*, 2019.

[77] R. K. Katzschmann, J. DelPreto, R. MacCurdy, and D. Rus, "Exploration of underwater life with an acoustically controlled soft robotic fish," *Science Robotics*, vol. 3, no. 16, p. eaar3449, 2018.

[78] B. J. Gemmell, J. H. Costello, S. P. Colin, C. J. Stewart, J. O. Dabiri, D. Tafti, and S. Priya, "Passive energy recapture in jellyfish contributes to propulsive advantage over other metazoans," *Proceedings of the National Academy of Sciences*, vol. 110, no. 44, pp. 17904–17909, 2013.

[79] A. Hoover and L. Miller, "A numerical study of the benefits of driving jellyfish bells at their natural frequency," *Journal of Theoretical Biology*, vol. 374, pp. 13–25, 6 2015.

[80] M. J. McHenry, "The ontogenetic scaling of hydrodynamics and swimming performance in jellyfish (aurelia aurita)," *Journal of Experimental Biology*, vol. 206, no. 22, pp. 4125–4137, 2003.

[81] J. Frame, N. Lopez, O. Curet, and E. D. Engeberg, "Thrust force characterization of free-swimming soft robotic jellyfish," *Bioinspiration & Biomimetics*, vol. 13, no. 6, p. 064001, 2018.

[82] J. C. Nawroth, H. Lee, A. W. Feinberg, C. M. Ripplinger, M. L. McCain, A. Grosberg, J. O. Dabiri, and K. K. Parker, "A tissue-engineered jellyfish with biomimetic propulsion," *Nature Biotechnology*, vol. 30, no. 8, pp. 792–797, 2012.

[83] Y. Tadesse, A. Villanueva, C. Haines, D. Novitski, R. Baughman, and S. Priya, "Hydrogen-fuel-powered bell segments of biomimetic jellyfish," *Smart Materials and Structures*, vol. 21, no. 4, 2012.

[84] A. Villanueva, C. Smith, and S. Priya, "A biomimetic robotic jellyfish (robojelly) actuated by shape memory alloy composite actuators," *Bioinspiration and Biomimetics*, vol. 6, no. 3, p. 036004, 2011.

[85] S. W. Yeom and I. K. Oh, "A biomimetic jellyfish robot based on ionic polymer metal composite actuators," *Smart Materials and Structures*, vol. 18, no. 8, 2009.

[86] Z. Ren, W. Hu, X. Dong, and M. Sitti, "Multi-functional soft-bodied jellyfish-like swimming," *Nature Communications*, vol. 10, no. 1, p. 2703, 2019.

[87] T. Cheng, G. Li, Y. Liang, M. Zhang, B. Liu, T.-W. Wong, J. Forman, M. Chen, G. Wang, Y. Tao, and T. Li, "Untethered soft robotic jellyfish," *Smart Materials and Structures*, vol. 28, p. 015019, 1 2019.

[88] C. Chiang Foo, S. Cai, S. Jin Adrian Koh, S. Bauer, and Z. Suo, "Model of dissipative dielectric elastomers," *Journal of Applied Physics*, vol. 111, no. 3, 2012.

[89] D. M. Opris, "Polar elastomers as novel materials for electromechanical actuator applications," *Advanced Materials*, vol. 30, no. 5, p. 1703678, 2018.

[90] B. Balakrisnan, A. Nacev, and E. Smela, "Design of bending multi-layer electroactive polymer actuators," *Smart Materials and Structures*, vol. 24, no. 4, p. 045032, 2015.

[91] D. Brown, "Tracker video analysis," 2019.

[92] T. Paschal, J. Shintake, S. Mintchev, and D. Floreano, "Development of bio-inspired underwater robot with adaptive morphology capable of multiple swimming modes," *IEEE International Conference on Intelligent Robots and Systems*, vol. 2017-Septe, pp. 4197–4202, 2017.

[93] R. F. Shepherd, A. A. Stokes, J. Freake, J. Barber, P. W. Snyder, A. D. Mazzeo, L. Cademartiri, S. A. Morin, and G. M. Whitesides, "Using explosions to power a soft robot," *Angewandte Chemie - International Edition*, vol. 52, no. 10, pp. 2892–2896, 2013.

[94] M. T. Tolley, R. F. Shepherd, M. Karpelson, N. W. Bartlett, K. C. Galloway, M. Wehner, R. Nunes, G. M. Whitesides, and R. J. Wood, "An untethered jumping soft robot," *IEEE International Conference on Intelligent Robots and Systems*, no. Iros, pp. 561–566, 2014.

[95] C. Laschi, B. Mazzolai, and M. Cianchetti, "Soft robotics: Technologies and systems pushing the boundaries of robot abilities," *Science Robotics*, vol. 1, no. 1, p. eaah3690, 2016.

[96] M. S. Triantafyllou and G. S. Triantafyllou, "An efficient swimming machine," *Scientific American*, vol. 272, no. 3, pp. 64–70, 1995.

[97] K. H. Low and A. Willy, "Biomimetic motion planning of an undulating robotic fish fin," *JVC/Journal of Vibration and Control*, vol. 12, no. 12, pp. 1337–1359, 2006.

[98] J. L. Tangorra, V. G. Lauder, I. W. Hunter, R. Mittal, P. G. A. Madden, and M. Bozkurttas, "The effect of fin ray flexural rigidity on the propulsive forces generated by a biorobotic fish pectoral fin," *Journal of Experimental Biology*, vol. 213, no. 23, pp. 4043–4054, 2010.

[99] A. Raj and A. Thakur, "Fish-inspired robots: design, sensing, actuation, and autonomy - a review of research," *Bioinspiration and Biomimetics*, vol. 11, no. 3, p. 031001, 2016.

[100] T. L. Daniel, "Mechanics and energetics of medusan jet propulsion," *Canadian Journal of Zoology*, vol. 61, no. 6, pp. 1406–1420, 2010.

[101] S. C. Steele, G. D. Weymouth, and M. S. Triantafyllou, "Added mass energy recovery of octopus-inspired shape change," *Journal of Fluid Mechanics*, vol. 810, pp. 155–174, 2017.

[102] M. S. Triantafyllou, G. D. Weymouth, and J. Miao, "Biomimetic survival hydrodynamics and flow sensing," *Annual Review of Fluid Mechanics*, vol. 48, no. 1, pp. 1–24, 2015.

[103] S. E. Spagnolie and M. J. Shelley, "Shape-changing bodies in fluid: Hovering, ratcheting, and bursting," *Physics of Fluids*, vol. 21, no. 1, pp. 1–13, 2009.

[104] S. Vogel, "Flow-assisted mantle cavity refilling in jetting squid," *The Biological Bulletin*, vol. 172, pp. 61–68, 2 1987.

[105] C. S. Wardle, "Limit of fish swimming speed," *Nature*, vol. 255, pp. 725–727, 6 1975.

[106] E. J. Anderson and M. A. Grosenbaugh, "Jet flow in steadily swimming adult squid," pp. 1125–1146, 2005.

[107] L. A. Ruiz, R. W. Whittlesey, and J. O. Dabiri, "Vortex-enhanced propulsion," *Journal of Fluid Mechanics*, vol. 668, pp. 5–32, 2011.

[108] R. W. Whittlesey and J. O. Dabiri, "Optimal vortex formation in a self-propelled vehicle," *Journal of Fluid Mechanics*, vol. 737, pp. 78–104, 2013.

[109] I. K. Bartol, P. S. Krueger, W. J. Stewart, and J. T. Thompson, "Hydrodynamics of pulsed jetting in juvenile and adult brief squid lolliguncula brevis: evidence of multiple jet 'modes' and their implications for propulsive efficiency," *Journal of Experimental Biology*, vol. 212, no. 12, pp. 1889–1903, 2009.

[110] G. Pawlak, C. Marugan Cruz, C. Martnez Bazn, and P. Garca Hrdy, "Experimental characterization of starting jet dynamics," *Fluid Dynamics Research*, vol. 39, pp. 711–730, 11 2007.

[111] J. M. Gosline and R. E. Shadwick, "The role of elastic energy storage mechanisms in swimming: an analysis of mantle elasticity in escape jetting in the squid, loligo opalescens," *Canadian Journal of Zoology*, vol. 61, pp. 1421–1431, 6 1983.

[112] K. C. Galloway, J. E. Clark, M. Yim, and D. E. Koditschek, "Experimental investigations into the role of passive variable compliant legs for dynamic robotic locomotion," *Proceedings - IEEE International Conference on Robotics and Automation*, pp. 1243–1249, 2011.

[113] J. O. Dabiri, "Optimal vortex formation as a unifying principle in biological propulsion," *Annual Review of Fluid Mechanics*, vol. 41, no. 1, pp. 17–33, 2008.

[114] Pololu, "20d metal gearmotors," 2019. [Online; accessed 2019-07-28].

[115] M. Rosenfeld, E. Rambod, and M. Gharib, "Circulation and formation number of laminar vortex rings," *Journal of Fluid Mechanics*, vol. 376, pp. 297–318, 1998.

[116] E. J. Anderson and M. E. DeMont, "The mechanics of locomotion in the squid loligo pealei: locomotory function and unsteady hydrodynamics of the jet and intramantle pressure.," *The Journal of experimental biology*, vol. 203, no. Pt 18, pp. 2851–63, 2000.

[117] Y. s. Yang, Y. c. Xie, and S. l. Nie, "Nozzle optimization for water jet propulsion with a positive displacement pump," *China Ocean Engineering*, vol. 28, no. 3, pp. 409–419, 2014.